

# Temporal Feature Matters: A Framework for Diffusion Model Quantization

Yushi Huang, Ruihao Gong, Xianglong Liu<sup>†</sup>, *Member, IEEE*, Jing Liu, Yuhang Li, Jiwen Lu, *Fellow, IEEE* and Dacheng Tao, *Fellow, IEEE*

**Abstract**—The Diffusion models, widely used for image generation, face significant challenges related to their broad applicability due to prolonged inference times and high memory demands. Efficient Post-Training Quantization (PTQ) is crucial to address these issues. However, unlike traditional models, diffusion models critically rely on the time-step for the multi-round denoising. Typically, each time-step is encoded into a hypersensitive temporal feature by several modules. Despite this, existing PTQ methods do not optimize these modules individually. Instead, they employ unsuitable reconstruction objectives and complex calibration methods, leading to significant disturbances in the temporal feature and denoising trajectory, as well as reduced compression efficiency. To address these challenges, we introduce a novel quantization framework that includes three strategies: 1) TIB-based Maintenance: Based on our innovative Temporal Information Block (TIB) definition, Temporal Information-aware Reconstruction (TIAR) and Finite Set Calibration (FSC) are developed to efficiently align original temporal features. 2) Cache-based Maintenance: Instead of indirect and complex optimization for the related modules, pre-computing and caching quantized counterparts of temporal features are developed to minimize errors. 3) Disturbance-aware Selection: Employ temporal feature errors to guide a fine-grained selection between the two maintenance strategies for further disturbance reduction. This framework preserves most of the temporal information and ensures high-quality end-to-end generation. Extensive testing on various datasets, diffusion models and hardware confirms our superior performance and acceleration.

**Index Terms**—Post-training Quantization, Diffusion Model, Temporal Feature, Hardware Acceleration.



## 1 INTRODUCTION

Generative modeling is pivotal in machine learning, particularly in applications like image [21], [22], [28], [64], [67], [75], voice [66], [73], and text synthesis [5], [89]. Diffusion models have demonstrated remarkable proficiency in generating high-quality samples across diverse domains. In comparison to generative adversarial networks (GANs) [15] and variational autoencoders (VAEs) [38], diffusion models successfully sidestep issues such as model collapse and posterior collapse, offering a more stable training regimen. However, the substantial computational cost [54], [84] poses a critical bottleneck hampering the widespread adoption of diffusion models. Specifically, this cost mainly stems from two primary factors. First, these models typically require hundreds of denoising steps to generate images, rendering the procedure considerably slower than that of GANs. Prior efforts [39], [48], [50], [75] have tackled this challenge by seeking shorter and more efficient sampling trajectories, thereby reducing the number of necessary denoising steps. Second, the substantial parameters and complex architec-

ture of diffusion models demand considerable time and memory resources for mobile device inference [6], [90], particularly for foundational models pre-trained on large-scale datasets, e.g., Stable Diffusion [67], SD-XL [64] and SD-XL-turbo [71]. Our work aims to address the latter challenge, focusing on the compression of diffusion models to enhance their efficiency and applicability.

Quantization, a technique for mapping high-precision floating-point numbers to lower-precision counterparts, stands as the most prevalent method for model compression [4], [11], [14], [57], [58]. Among different quantization paradigms, post-training quantization (PTQ) [24], [57], [81] incurs lower overhead and is more user-friendly without the need for retraining or fine-tuning with a huge amount of training data. While PTQ on conventional models has undergone extensive study [14], [43], [57], [81], its adaptation to diffusion models has shown huge performance degradation, especially under low-bit settings. For instance, Q-Diffusion [42] exhibits 6.81 Fréchet Inception Distance (FID) [20] increasing on CelebA-HQ  $256 \times 256$  [31] under 4-bit weight and 8-bit activation quantization. We believe the reason they fail to achieve better results is that they all overlook the sampling data independence and uniqueness of hypersensitive temporal features, which are generated from time-step  $t$  through a few modules, used to control the denoising trajectory in diffusion models. As a result, the temporal feature disturbance stemming from quantization significantly impacts model performance in the existing studies.

To tackle temporal feature disturbance, we first find that the modules generating temporal features are independent

- Y. Huang, and R. Gong are with SenseTime Research, China.
- R. Gong, and X. Liu are with the State Key Laboratory of Software Development Environment, Beihang University, China.
- J. Liu is with the Department of Data Science and AI, Faculty of IT, Monash University, Australia.
- Y. Li is with the Electrical Engineering Department at Yale University, America.
- J. Lu is with the Department of Automation, Tsinghua University, China.
- D. Tao is with the School of Computer Science and Engineering at Nanyang Technological University, Singapore.
- †: Corresponding author.

of the sampling data and thus treat the whole modules as the Temporal Information Block (TIB). However, existing methods [18], [42], [72], [74], [77] do not separately optimize this block during the quantization process, causing temporal features to overfit to limited calibration data. Additionally, since the maximum time-step for denoising is a finite positive integer, the temporal feature and the activations during its generation form a finite set. Therefore, the optimal approach is to optimize each element in this set individually. Inspired by these observations and analyses, we propose two temporal feature maintenance techniques: 1) **TIB-based Maintenance**: Based on TIB, a novel quantization reconstruction approach, Temporal Information-aware Reconstruction (TIAR), is devised. It aims to reduce temporal feature error as the optimization objective while isolating the network’s components related to sampled data during weight adjustment. Besides, we also introduce a calibration strategy, Finite Set Calibration (FSC), for the finite set of the temporal feature and activation during its generation. 2) **Cache-based Maintenance**: Further leveraging the independent and finite nature of the temporal feature, we directly pre-compute these features, and then optimize and cache their quantized versions to reduce the disturbance. In detail, this novel design only requires reloading cached features, avoiding online generation during inference, which enhances latency in specific cases. Moreover, we employ our **Disturbance-aware Selection** taking advantage of both maintenance approaches to further eliminate temporal feature error. In addition, only one offline generation process for fine-grained maintenance strategies chosen ensured the efficiency of our selection scenario. Finally, evaluating on multiple datasets, diverse tasks, advanced models, and different hardware, our novel framework towards reducing temporal feature disturbance achieved nearly lossless model compression with high inference speed.

In summary, our contributions are as follows:

- We discover that existing quantization methods suffer from hypersensitive temporal feature disturbances and mismatched problem, which disrupt the denoising trajectory of diffusion models and significantly affect the quality of generated images.
- We reveal that the disturbance comes from two sources: an inappropriate reconstruction target and a lack of awareness of finite activations. Both inducements ignore the special characteristics of modules related to temporal information.
- We propose an advanced quantization framework, consisting of 1) TIB-based Maintenance: Temporal Information-aware Reconstruction (TIAR) and Finite Set Calibration (FSC). Both are based on a Temporal Information Block specially defined for diffusion models. 2) Cache-based Maintenance: Directly optimize and save quantized temporal feature, and then reload for inference. 3) Disturbance-aware Selection: fine-grained select our maintenance strategies offline employing temporal feature error.
- Extensive experiments demonstrate our superior performance. For example, our framework reduces the FID score by 5.61 under the w4a8 configuration for SD-XL [64]. Additionally, we deploy the

quantized model on different hardware to demonstrate the inference acceleration, *e.g.*,  $2.20\times$  and  $5.76\times$  speedup on Intel<sup>®</sup> Xeon<sup>®</sup> Gold 6448Y Processor and Nvidia H800 GPU for SD-XL, respectively.

This paper extends our conference version [23] in several aspects. 1) We compare and fine-grainedly analyze the sensitivity and quantization-induced disturbance between temporal features and other non-temporal features. 2) We propose Cache-based Maintenance parallel to TIB-based Maintenance with high efficiency. It can achieve comparable performance and even lower inference costs in some cases. 3) We propose Disturbance-aware Selection fine-grainedly harness both maintenance strategies to further reduce disturbance in temporal features. 4) We apply our framework to advanced Text-to-Image (T2I) models, *e.g.*, SD-XL [64] and SD-XL-turbo [71]. 5) We deploy our quantized model employing CUTLASS [32] with our customized kernel on Nvidia H800 GPU and OpenVino [25] on Intel<sup>®</sup> Xeon<sup>®</sup> Gold 6448Y Processor to show significant acceleration. 6) We provide comprehensive experiments and more ablation studies to investigate the effectiveness of our methods.

## 2 RELATED WORK

### 2.1 Efficient Diffusion Models

Diffusion models have demonstrated the ability to generate high-quality images. However, their extensive iterative process coupled with the computational cost of denoising via networks has impeded wide-ranging applications. To tackle this challenge, prior research has explored efficient methods to expedite the denoising process [1], [35], [80], [82]. These methods fall into two categories: those requiring re-training and advanced samplers tailored for pre-trained models. The former category includes techniques like diffusion process learning [8], [13], [53], [91], noise scale adaptation [37], [60], knowledge distillation [34], [52], [70], and sample trajectory refinement [41], [59], [80]. While these methods can speed up sampling, re-training a diffusion model proves resource-intensive and time-consuming. In contrast, the latter category involves designing efficient samplers for pre-trained diffusion models, eliminating the need for re-training. Key methods in this category encompass analytical trajectory estimation [2], [3], implicit samplers [39], [75], [88], and differential equation (DE) solvers such as customized stochastic differential equations (SDE) [27], [33], [76] and ordinary differential equations (ODE) [48], [50], [87]. While these approaches can reduce sampling iterations, diffusion models’ extensive parameters, and computational complexity restrict their deployment in real-world settings. In this paper, our work focuses on diminishing the time and memory overhead of the single-step denoising process using low-bit quantization in a post-training manner, a method orthogonal to previous speedup techniques.

### 2.2 Model Quantization

Quantization is a predominant technique for minimizing storage and computational costs. It can be categorized into quantization-aware training (QAT) [14], [26], [49], [86], [93] and post-training quantization (PTQ) [24], [43], [46], [57], [81]. QAT requires intensive model training with substantial

data and computational demands. Correspondingly, PTQ compresses models without re-training, making it a preferred method due to its minimal data requirements and easy deployment on real hardware. In PTQ, given a high-precision value  $x$ , we map it into discrete one  $\hat{x}$  using uniform quantization expressed as:

$$\hat{x} = \Phi\left(\left\lfloor \frac{x}{s} \right\rfloor + z, 0, 2^b - 1\right), \quad (1)$$

where  $s$  is the quantization step size,  $z$  is the zero offset, and  $b$  is the target bit-width. The clamp function  $\Phi(\cdot)$  clips the rounded value  $\left\lfloor \frac{x}{s} \right\rfloor + z$  within the range of  $[0, 2^b - 1]$ . However, naive quantization may lead to accuracy degradation, especially for low-bit quantization. Recent studies [12], [43], [44], [47] have explored innovative strategies based on reconstruction to preserve model performance after low-bit quantization. For instance, AdaRound [57] extends PTQ to 4-bit on traditional vision models using a novel rounding mechanism with layer-wise reconstruction [24], [79]. BRECQ [43] balances cross-layer dependency and generalization error by leveraging neural network blocks and employing block-wise reconstruction. Additionally, QDrop [81], considering the impact of activation quantization when reconstructing layer/block outputs.

In contrast, the iterative denoising process in diffusion models presents new challenges for PTQ in comparison to traditional models. PTQ4DM [72] represents the initial attempt to quantize diffusion models to 8-bit, albeit with limited experiments and lower resolutions. Conversely, Q-Diffusion [42] achieves enhanced performance and is evaluated on a broader dataset range. Moreover, PTQD [18] eliminates quantization noise through correlated and residual noise correction. Notably, traditional single-time-step PTQ calibration methods are unsuitable for diffusion models due to significant activation distribution changes with each time-step [42], [72], [74], [77]. ADP-DM [77] proposes group-wise quantization across time-steps for diffusion models, and TDQ [74] introduces distinct quantization parameters for different time-steps. However, all of the above works overlook the specificity of hypersensitive temporal features. To address temporal feature disturbance in the aforementioned works, our study delves into the inducements of the phenomenon and introduces a novel PTQ framework for diffusion models, significantly enhancing quantized diffusion model performance.

### 3 PRELIMINARIES

**Diffusion models.** Diffusion models [21], [75] iteratively add Gaussian noise with a variance schedule  $\beta_1, \dots, \beta_T \in (0, 1)$  to data  $\mathbf{x}_0 \sim q(\mathbf{x})$  for  $T$  times as sampling process, resulting in a sequence of noisy samples  $\mathbf{x}_1, \dots, \mathbf{x}_T$ . In DDPMs [21], the former sampling process is a Markov chain, taking the form:

$$q(\mathbf{x}_{1:T}|\mathbf{x}_0) = \prod_{t=1}^T q(\mathbf{x}_t|\mathbf{x}_{t-1}), \quad (2)$$

$$q(\mathbf{x}_t|\mathbf{x}_{t-1}) = \mathcal{N}(\mathbf{x}_t; \sqrt{\alpha_t}\mathbf{x}_{t-1}, \beta_t\mathbf{I}),$$

where  $\alpha_t = 1 - \beta_t$ . Conversely, the denoising process removes noise from a sample from Gaussian noise  $\mathbf{x}_T \sim$

$\mathcal{N}(\mathbf{0}, \mathbf{I})$  to gradually generate high-fidelity images. Nevertheless, due to the unavailability of the true reverse conditional distribution  $q(\mathbf{x}_{t-1}|\mathbf{x}_t)$ , diffusion models approximate it via variational inference by learning a Gaussian distribution  $p_\theta(\mathbf{x}_{t-1}|\mathbf{x}_t) = \mathcal{N}(\mathbf{x}_{t-1}; \boldsymbol{\mu}_\theta(\mathbf{x}_t, t), \boldsymbol{\Sigma}_\theta(\mathbf{x}_t, t))$ , the  $\boldsymbol{\mu}_\theta$  can be derived by reparameterization trick as follows:

$$\boldsymbol{\mu}_\theta(\mathbf{x}_t, t) = \frac{1}{\sqrt{\alpha_t}} \left( \mathbf{x}_t - \frac{\beta_t}{\sqrt{1 - \bar{\alpha}_t}} \boldsymbol{\epsilon}_\theta(\mathbf{x}_t, t) \right), \quad (3)$$

where  $\bar{\alpha}_t = \prod_{i=1}^t \alpha_i$  and  $\boldsymbol{\epsilon}_\theta(\cdot)$  is a noise estimation model. The variance  $\boldsymbol{\Sigma}_\theta(\mathbf{x}_t, t)$  can be either learned [60] or fixed to a constant schedule [21]  $\sigma_t$ . When employing the latter method,  $\mathbf{x}_{t-1}$  can be expressed as:

$$\mathbf{x}_{t-1} = \frac{1}{\sqrt{\alpha_t}} \left( \mathbf{x}_t - \frac{\beta_t}{\sqrt{1 - \bar{\alpha}_t}} \boldsymbol{\epsilon}_\theta(\mathbf{x}_t, t) \right) + \sigma_t \mathbf{z}, \quad (4)$$

where  $\mathbf{z} \sim \mathcal{N}(\mathbf{0}, \mathbf{I})$ .

**Reconstruction on diffusion models.** Depicted in Fig. 1, UNet architecture [68], the predominant model employed as  $\boldsymbol{\epsilon}_\theta(\cdot)$  in Eq. (4) to predict Gaussian noise, can be divided into blocks that incorporate residual connections (such as Residual Bottleneck Blocks or Transformer Blocks [63]) and the remaining layers. Numerous PTQ techniques for diffusion models are grounded in layer/block-wise reconstruction [18], [42], [72], [74] to learn optimal quantization parameters. For example, in the Residual Bottleneck Block, this approach typically minimizes the loss function as follows:

$$\mathcal{L}_i = \|f_i(\cdot) - \hat{f}_i(\cdot)\|_F^2, \quad (5)$$

where  $\|\cdot\|_F^2$  denotes the Frobenius norm. The function  $f_i(\cdot)$  represents the  $i^{\text{th}}$  Residual Bottleneck Block, and  $\hat{f}_i(\cdot)$  denotes its quantized counterpart. Furthermore, in the following sections, we use  $n$  to denote the total number of Residual Bottleneck Blocks in a single diffusion model. Unless otherwise stated, we adopt the aforementioned method as our baseline in Sec. 4.

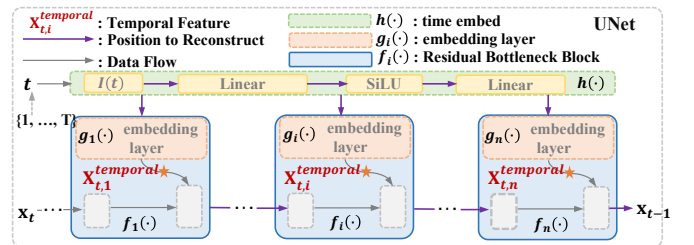


Fig. 1: UNet architecture with a single denoising process at  $t$ . We omit the Transformer Blocks, some convolutions, and the sampler in the figure.

**Temporal feature in diffusion models.** Also shown in Fig. 1, time-step  $t$  is encoded with time embed<sup>1</sup> and then passes through the embedding layer<sup>2</sup> in each Residual Bottleneck Block, resulting in a series of unique activations. In this paper, we denote these activations as temporal features. Notably, temporal features are independent of  $\mathbf{x}_t$  and

1. PyTorch time embed implementation in diffusion models.
2. PyTorch embedding layer implementation in diffusion models.



unrelated to other temporal features from different time-steps. For enhanced clarity in our notation: the time embed function is denoted as  $h(\cdot)$ , the embedding layer within the  $i^{\text{th}}$  Residual Bottleneck Block as  $g_i(\cdot)$ , and the resultant  $i^{\text{th}}$  temporal feature at time-step  $t$  as  $\mathbf{X}_{t,i}^{\text{temporal}}$ . Moreover, as illustrated in Fig. 1, the relationship among these components is expressed as

$$\mathbf{X}_{t,i}^{\text{temporal}} = g_i(h(t)) \quad (6)$$

Additionally, we have found that temporal features play a crucial role in the context of the diffusion model as they hold unique and substantial physical implications. These features contain temporal information that indicates the current image’s position along the denoising trajectory. Within the architecture of the UNet, each time-step is converted into these temporal features, which then guide the denoising process by applying them to the features of images generated in successive iterations.

## 4 TEMPORAL FEATURE MATTERS

We organize this section as follows. Firstly, we observe the disturbance induced by the previous method of the highly sensitive temporal feature in Sec. 4.1. Further findings in Sec. 4.2 confirm the drastic impact. Concurrently, we analyze the inducements in Sec. 4.3. Finally, we propose our quantization framework in Sec. 4.4.

### 4.1 Disturbance Observations

Based on Sec. 3, we investigate how temporal features exhibit salient sensitivity of disturbance, and then we identify the phenomenon of temporal feature disturbance induced by quantization.

**Temporal feature sensitivity.** Beyond the special physical significance of temporal feature on image generation, we find these features are more sensitive than others (*i.e.*, other activations in the model can endure greater disturbances with minimal impact on performance). To validate this, we first introduce non-temporal features  $\mathbf{X}_{t,i}^{\text{non-temporal}}$  to represent activations except temporal features for every time-step  $t$ . Then, we randomly select  $n$  non-temporal features<sup>3</sup> at  $t$ , and apply varying levels of random Gaussian noise to both (*i.e.*, temporal and non-temporal features). The noise can be formulated as follows:

$$\Delta_\lambda = \lambda \Delta \quad (7)$$

where  $\lambda$  represents the noise level for the model.  $\Delta \sim \mathcal{N}(\mu, \sigma^2)$ , where  $\mu$  and  $\sigma^2$  denote mean and variance for the corresponding temporal/non-temporal feature, respectively. As shown in Fig. 2, the FID deteriorates sharply with increasing  $\lambda$  when disturbances are applied to the temporal features, in contrast to a gradual increase observed for random non-temporal features.

**Temporal feature disturbance.** Having established the sensitivity of the temporal feature to disturbance, we thoroughly analyze its variations before and after the quantization of embedding layers and time embed in the

3. Hence, here  $i = 1, \dots, n$ , the same for the temporal feature.

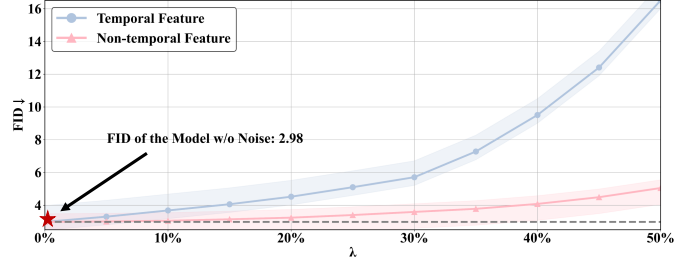


Fig. 2: FID [20] on LSUN-Bedrooms 256 × 256 [85] for LDM-4, with Gaussian noise applied to its temporal/non-temporal features activations.

Stable Diffusion model. Prior to this analysis, we introduce the temporal/non-temporal feature activation error at  $t$  as defined by:

$$E_t^* = \frac{\sum_{i=1}^n \cos(\mathbf{X}_{t,i}^*, \widehat{\mathbf{X}}_{t,i}^*)}{n}, \quad (8)$$

where  $*$  can be “temporal” or “non-temporal”,  $\cos(\cdot)$  denotes cosine similarity, and  $\widehat{\mathbf{X}}_{t,i}^*$  signifies the temporal/non-temporal feature corresponding to  $\mathbf{X}_{t,i}^*$  in the quantized model. Notably, sample-independent temporal features do not have cumulative error from the iterative quantized denoising process. Conversely, to eliminate the cumulative error amplifying the quantization error, we employ the full-precision denoising from  $T$  to  $t + 1$  to get the input  $\mathbf{x}_t$ , and then fetch  $\{\mathbf{X}_{t,i}^{\text{non-temporal}}\}_{i=1,\dots,n}$  from the quantized denoising at  $t$ . As illustrated in Fig. 3 (Left), quantization

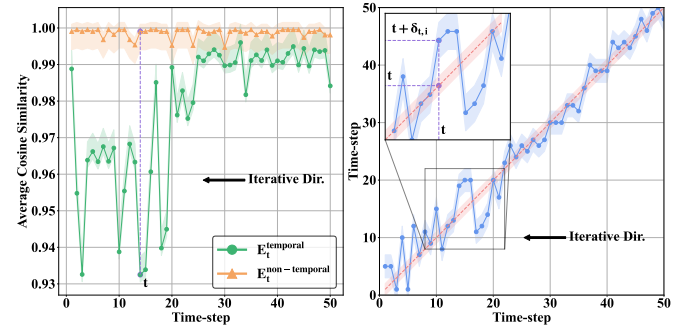


Fig. 3: (Left) Temporal feature disturbance. The green inflection points highlight the significant phenomenon of temporal feature disturbance. (Right) Temporal information mismatch ( $i = 11$ ). The coordinates of the inflection points on the blue curve can denoted as  $(t, t + \delta_{t,i})$ . It indicates  $\widehat{\mathbf{X}}_{t,i}^{\text{temporal}}$  exhibits the highest similarity with  $\mathbf{X}_{t+\delta_{t,i},i}^{\text{temporal}}$ .

induces notable errors in temporal features, far exceeding those in non-temporal ones. We refer to this phenomenon, characterized by substantial temporal feature errors within diffusion models, as temporal feature disturbance.

### 4.2 Disturbance Impacts

In addition to the intense disturbances caused by previous quantization approaches to highly sensitive temporal features, we further explore their subsequent impacts.



**Temporal information mismatch.** Obviously, temporal feature disturbance alters the original embedded temporal information. Specifically,  $\mathbf{X}_{t,i}^{temporal}$  is intended to correspond to time-step  $t$ . However, due to significant errors, the quantized model’s  $\widehat{\mathbf{X}}_{t,i}^{temporal}$  is no longer accurately associated with  $t$ , resulting in what we term as temporal information mismatch:

$$t \leftarrow \mathbf{X}_{t,i}^{temporal}, \quad t \leftarrow \widehat{\mathbf{X}}_{t,i}^{temporal}. \quad (9)$$

Furthermore, as depicted in Fig. 3 (Right), we even observe a pronounced temporal information mismatch in Stable Diffusion. Specifically, the temporal feature generated by the quantized model at time-step  $t$  exhibits a divergence from that of the full-precision model at the corresponding time-step. Instead, it tends to align more closely with the temporal feature corresponding to  $t + \delta_t$ , importing wrong temporal information from  $t + \delta_t$ .

**Trajectory deviation.** Temporal information mismatch delivers wrong temporal information, therefore, causing a deviation in the corresponding temporal position of the image within the denoising trajectory, ultimately leading to:

$$\mathbf{x}_t \not\Rightarrow \mathbf{x}_{t-1}, \quad (10)$$

where we apply disrupted temporal features to the model. Evidently, the deviation in the denoising trajectory intensifies as the number of denoising iterations increases, resulting in the final generated image failing to align accurately with  $\mathbf{x}_0$ . This evolution is illustrated in Fig. 4, where we maintain UNet in full precision, except for embedding layers and time embed.



Fig. 4: Denoising process of full-precision (Upper) and w4a8 quantized (Lower) Stable Diffusion ( $T = 50$ ) under the same experiment settings,  $\mathbf{x}_0$ . It is noteworthy that, in the quantized model employed here, to showcase the impact of temporal features, only the layers generating temporal features are quantized and the components unrelated to the generation of temporal features are maintained in full precision.

### 4.3 Inducement Analyses

In this section, we explore the two inducements of temporal feature disturbance. For the purpose of clarity, in the subsequent sections, “reconstruction” specifically points to slight weight adjustment for minimal quantization error, while “calibration” specifically refers to activation calibration.

**Inappropriate reconstruction target.** Previous PTQ methods [18], [42], [74] have achieved remarkable progress on diffusion models. However, these existing methods overlook the temporal feature’s independence and its distinctive physical significance. In their reconstruction processes, there was a lack of optimization for the embedding layers. Instead, a Residual Bottleneck Block of coarser granularity was selected as the reconstruction target as depicted in Fig. 1. This method involves two potential factors causing temporal feature disturbance: 1) Optimize the objective as expressed in Eq. (5) to decrease the reconstruction loss of the Residual Bottleneck Block, as opposed to directly alleviating temporal feature disturbance. 2) During backpropagation of the reconstruction process, embedding layers independent from  $\mathbf{x}_t$  are affected by  $\mathbf{x}_t$ , resulting in an overfitting scenario on limited calibration data.

To further substantiate our analyses, we compare the above-mentioned reconstruction method, e.g., BRECC [43] with the approach where the parameters of the embedding layers were frozen during the reconstruction of the Residual Bottleneck Block and initialized solely through Min-max [58]. As shown in Tab. 1, the Freeze strategy exhibits superior results, which verify that embedding layers served as their own optimization objective and maintaining their independence of  $\mathbf{x}_t$  can significantly mitigate temporal feature disturbance, particularly at low-bit.

TABLE 1: FID, sFID and SQNR on LSUN-Bedrooms  $256 \times 256$  [85] for LDM-4. Prev represents BRECC. Freeze denotes our trial.

Methods	#Bits (W/A)	FID↓	sFID↓	SQNR↑
Full Prec.	32/32	2.98	7.09	-
Prev	8/8	7.51	12.54	-0.12
Freeze	8/8	5.76 <sub>-1.75</sub>	8.42 <sub>-4.12</sub>	4.07 <sub>+4.19</sub>
Prev	4/8	9.36	22.73	-1.61
Freeze	4/8	7.08 <sub>-2.28</sub>	16.82 <sub>-5.91</sub>	3.42 <sub>+5.03</sub>

**Unaware of finite activations within  $h(\cdot)$  and  $g_i(\cdot)$ .** We observe that, given  $T$  as a finite positive integer, the set of all possible activation values for embedding layers and time embed is finite and strictly dependent on time-steps. Within this set, activations corresponding to the same layer display notable range variations across different time-steps<sup>4</sup>. Previous methods [74], [77] mainly focus on finding the optimal calibration method for  $\widehat{\mathbf{x}}_t$ -related network components. Moreover, akin to the first inducement, their calibration is directly towards the Residual Bottleneck Block, which proves suboptimal<sup>5</sup>. However, based on the finite activations, we can employ calibration methods, especially for these time information-related activations, to better adapt to their range variations.

### 4.4 Quantization Framework

To mitigate temporal feature disturbance, we propose two different temporal feature maintenance strategies categorized into TIB-based and cache-based ones in Sec. 4.4.1

<sup>4</sup> The details of range variations can be found in Sec. B in the appendix of [23]

<sup>5</sup> The evidence can be found in Sec. C in the appendix of [23]

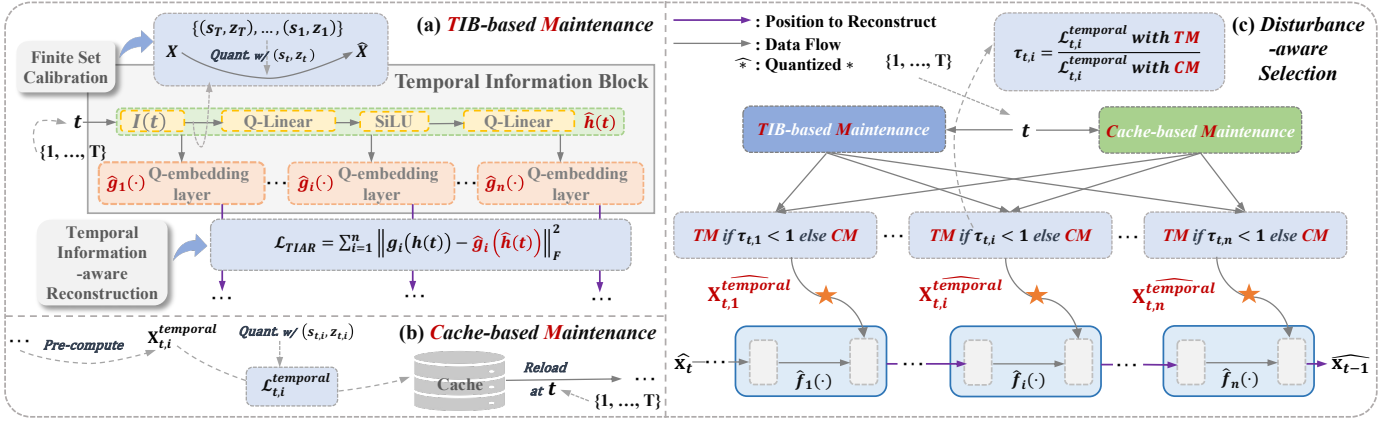


Fig. 5: Overview of the proposed framework. (a) **TIB-based Maintenance**: Based on a Temporal Information Block, we enable Temporal Information-aware Reconstruction and Finite Set Calibration. (b) **Cache-based Maintenance**: We directly quantize these temporal features and reload them for inference. (c) **Disturbance-aware Selection**: We select the appropriate maintenance through temporal feature error for further improvement. This framework achieves the maintenance of temporal features and yields promising results.

and Sec. 4.4.2, respectively. Finally, we incorporate both scenarios together with our selection strategy to further solve the problem in Sec. 4.4.3. Our methods are outlined in Fig. 5.

#### 4.4.1 TIB-based Maintenance

Referring to the two inducements aforementioned, we define a novel Temporal Information Block (TIB) to maintain the temporal features. Built on the block, Temporal Information-aware Reconstruction and Finite Set Calibration are proposed to solve the two inducements analyzed above.

**Temporal Information Block (TIB)**. Based on the inducements, it is crucial to meticulously separate the reconstruction and calibration process for each embedding layer and Residual Bottleneck Block to enhance quantized model performance. Considering the unique structure of the UNet, we consolidate all embedding layers and time embed into a unified Temporal Information Block (TIB), which can be denoted as  $\{g_i(h(\cdot))\}_{i=0,\dots,n}$  (see Fig. 5 (a)).

**Temporal Information-aware Reconstruction**. Based on the Temporal Information Block (TIB), we introduce the Temporal Information-aware Reconstruction (TIAR) to address the first inducement. The optimization goal for the block during the reconstruction phase is captured by the following loss function

$$\mathcal{L}_{TIAR} = \sum_{i=0}^n \|g_i(h(t)) - \hat{g}_i(\hat{h}(t))\|_F^2, \quad (11)$$

where  $\hat{h}(\cdot)$  and  $\hat{g}_i(\cdot)$  represent the quantized counterparts of  $h(\cdot)$  and  $g_i(\cdot)$ , respectively. This reconstruction strategy focuses on adjusting weights to pursue a minimal disturbance for temporal features.

**Finite Set Calibration**. To address the challenge posed by the wide span of activations within a finite set for the second inducement, we propose Finite Set Calibration (FSC) for activation quantization. This strategy employs  $T$  sets

of quantization parameters for every activation within all the embedding layers and time embed, such as  $\{(s_T, z_T), \dots, (s_1, z_1)\}$  for activation  $\mathbf{X}$ . At time-step  $t$ , the quantization function for the  $\mathbf{X}$  can be expressed as:

$$\hat{\mathbf{X}} = \Phi\left(\left\lfloor \frac{\mathbf{X}}{s_t} \right\rfloor + z_t, 0, 2^b - 1\right), \quad (12)$$

where  $s_t$  and  $z_t$  are the corresponding scale and zero offset. To be noted, the calibration target for these activations is also aligned with the output of the TIB. Besides that, we find that Min-max [58] can achieve satisfactory results with high efficiency (more evidence in Sec. 5.4.2) for range estimation. In Sec. 5.3.1, we perform a detailed analysis to demonstrate that our method incurs a negligible extra cost for inference.

#### 4.4.2 Cache-based Maintenance

Further considering sample independence and finitude of the temporal feature, the feature associated with each  $t$  and  $i$  remains constant and can therefore be pre-computed offline. This allows us to directly optimize the quantization parameters for these pre-computed features and cache the quantized counterparts with the parameters to address the issues. The objective for all  $t$  and  $i$  can be formulated as follows:

$$\arg \min_{s_{t,i}, z_{t,i}} \underbrace{\|\mathbf{X}_{t,i}^{\widehat{temporal}} - \mathbf{X}_{t,i}^{temporal}\|_F^2}_{\mathcal{L}_{t,i}^{temporal}}, \quad (13)$$

where  $s_{t,i}$  and  $z_{t,i}$  denote quantization scale and zero offset for the pre-gained  $\mathbf{X}_{t,i}^{temporal}$ . Moreover, we employ LSQ [11] to optimize every objective separately, which can be done in just a few minutes. During inference, this strategy enables us to get the temporal feature by reloading the cached items. In addition, we find that this approach can help improve latency. More detailed analysis can be found in Sec. 5.3.2.

#### 4.4.3 Disturbance-aware Selection

We visualize the comparison of the temporal feature disturbance between the two maintenance approaches in Fig. 6,

where the grid value of  $(t, i)$  represents the temporal feature error<sup>6</sup> as follows:

$$\tau_{t,i} = \frac{\mathcal{L}_{t,i}^{temporal} \text{ with TIB-based Maintenance}}{\mathcal{L}_{t,i}^{temporal} \text{ with Cache-based Maintenance}}. \quad (14)$$

Given the discrepancy in temporal feature errors across dif-

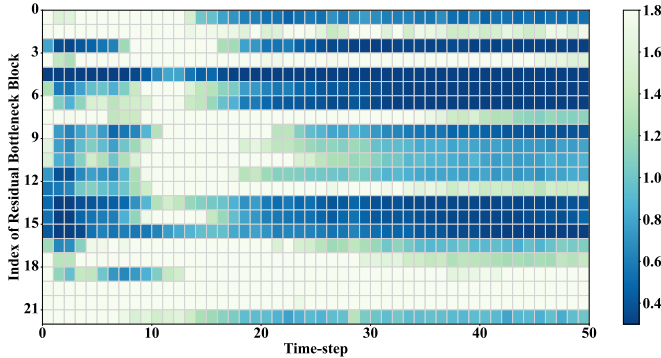


Fig. 6: Comparison of the temporal feature disturbance between TIB-based and Cache-based Maintenance with w4a8 quantized Stable Diffusion ( $T = 50$ ).

ferent  $t$  and  $i$  in our two methods, we propose Disturbance-aware Selection to better mitigate the temporal feature disturbance. Specifically, when  $\tau_{t,i} < 1$ , we employ TIB-based Maintenance to obtain  $\mathbf{X}_{t,i}^{temporal}$ . Conversely, we opt for Cache-based Maintenance. For efficiency, our selection procedure can be done offline with only one image generation pass. To validate its performance, Fig. 7 demonstrates that our straightforward but effective selection strategy successfully leverages the strengths of both maintenance approaches.

*“A small, neat, simple kitchen with lots of cupboards and a small work table in the middle of the room.”*

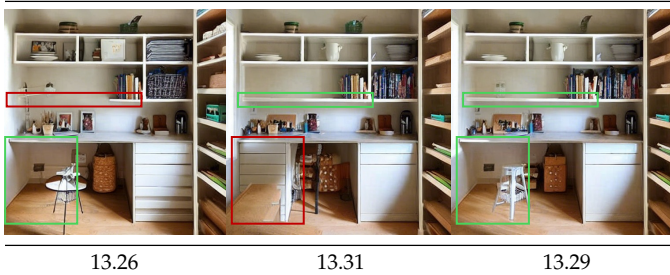


Fig. 7: Samples from w4a8 quantized Stable Diffusion on MS-COCO [45] caption with TIB-based Maintenance (Left), Cache-based Maintenance (Middle), and Disturbance-aware Selection (Right), where **green rectangles** present finer points than **red rectangles**. Numbers in the last row denote FID on MS-COCO caption of the corresponding methods.

## 5 EXPERIMENTS

We organize the experiments as follows: In Sec. 5.1, we first demonstrate implementation details. Then, we exhibit

6. Here we employ  $\mathcal{L}_{t,i}^{temporal}$  in Eq. (13), instead of that in Eq. (8) as temporal feature error, since over 82% of cosine similarity with our two maintenance approaches are almost exactly equal to 1, which shows the remarkable effect of our methods.

the outstanding performance gained by our framework in Sec. 5.2. Further, we also deploy our quantized models on various hardware to investigate their inference efficiency in Sec. 5.3. Last, we conduct comprehensive ablative studies for the proposed framework in Sec. 5.4.

### 5.1 Implementation details

**Models and datasets.** In this section, we conduct image generation experiments to evaluate the proposed quantization framework on various diffusion models: pixel-space diffusion model DDPM [21] for unconditional image generation, latent-space diffusion model LDM [67] for unconditional image generation and class-conditional image generation. We also apply our work to Stable Diffusion-v1-4 [67], SD-XL-base-1.0 [64], and SD-XL-turbo [71] for text-guided image generation. In our experiments, We use seven standard benchmarks: CIFAR-10  $32 \times 32$  [40], LSUN-Bedrooms  $256 \times 256$  [85], LSUN-Churches  $256 \times 256$  [85], CelebA-HQ  $256 \times 256$  [29], ImageNet  $256 \times 256$  [9], FFHQ  $256 \times 256$  [31] and MS-COCO [45].

**Quantization settings.** We use channel-wise quantization for weights and tensor-wise quantization for activations, as it is a common practice. In our experimental setup, we employ BRECQ [43] and AdaRound [57]. Drawing from empirical insights derived from conventional model quantization practices [16], [65], we maintain the input and output layers of the model in full precision. Mirroring the details outlined in Q-Diffusion [42]<sup>7</sup>, we generate calibration data through full-precision diffusion models. Moreover, for weight quantization, we reconstruct quantized weights for 20k iterations with a mini-batch size of 32 for DDPM and LDM, 8 for Stable Diffusion and SD-XL-turbo, and 4 for SD-XL. For activation quantization, we utilize EMA [26] to estimate the ranges of activations, also equipping the paradigm from [17], [74], [78]. This stage applies a mini-batch size of 16 for all models. To be noted, we follow the block-wise reconstruction in [18], [42]. For Cache-based Maintenance, we employ LSQ [4] for 10k iterations to quantize pre-fetched features in 8-bit for all configurations, including weight-only quantization.

**Evaluation metrics.** For each experiment, we evaluate the performance of diffusion models with Fréchet Inception Distance (FID) [20], and Signal-to-quantization-noise Ratio (SQNR) [61] which measures the quantization distortion in detail. In the case of LDM and text-guided generation experiments, we also include sFID [69], which better captures spatial relationships than FID. For ImageNet and CIFAR-10 experiments, we additionally provide Inception Score (IS) [69] as a reference metric. Further, in the context of text-guided experiments, we extend our evaluation to include the compatibility of image-caption pairs, employing the CLIP score [19]. The ViT-B/32 [10] is used as the backbone when computing the CLIP score. To ensure consistency in the reported outcomes, all results are derived from our implementation or from other papers, where experiments are conducted under conditions consistent with ours. More

7. This can be found in the appendix of [42]. For SD-XL and SD-XL-turbo, we collect 8 and 1024 COCO prompts, respectively.



TABLE 2: Quantization results for unconditional image generation with LDM-4 on LSUN-Bedrooms  $256 \times 256$ , FFHQ  $256 \times 256$  and CelebA-HQ  $256 \times 256$ , LDM-8 on LSUN-Churches  $256 \times 256$ . “\*” represents our implementation according to open-source codes and “+” means directly rerunning open-source codes. The subscript numbers represent the improvements from our framework compared with the previous methods. Blue/Green color is to represent the negative/positive number. “TM” is TIB-based Maintenance, “CM” is Cache-based Maintenance, and “DS” denotes our Disturbance-aware Selection.

Methods	#Bits (W/A)	LSUN-Bedrooms $256 \times 256$			LSUN-Churches $256 \times 256$			CelebA-HQ $256 \times 256$			FFHQ $256 \times 256$		
		FID↓	sFID↓	SQNR↑	FID↓	sFID↓	SQNR↑	FID↓	sFID↓	SQNR↑	FID↓	sFID↓	SQNR↑
Full Prec.	32/32	2.98	7.09	-	4.12	10.89	-	8.74	10.16	-	9.36	8.67	-
PTQ4DM* [72]	4/32	4.83	7.94	4.47	4.92	13.94	0.62	13.67	14.72	4.18	11.74	12.18	-2.87
Q-Diffusion† [42]	4/32	4.20	7.66	5.11	4.55	11.90	1.22	11.09	12.00	5.67	11.60	10.30	-2.04
PTQD* [18]	4/32	4.42	7.88	4.89	4.67	13.68	1.15	11.06	12.21	5.52	12.01	11.12	-2.36
TM	4/32	3.60 <sub>-0.60</sub>	7.61 <sub>-0.05</sub>	8.45 <sub>+3.34</sub>	4.07 <sub>-0.48</sub>	11.41 <sub>-0.49</sub>	2.21 <sub>+0.99</sub>	8.74 <sub>-2.32</sub>	10.18 <sub>-1.82</sub>	6.93 <sub>-1.26</sub>	9.89 <sub>-1.71</sub>	9.06 <sub>-1.24</sub>	-1.98 <sub>+0.06</sub>
CM	4/32	3.58 <sub>-0.62</sub>	7.42 <sub>-0.24</sub>	7.72 <sub>+2.61</sub>	4.10 <sub>-0.45</sub>	11.23 <sub>-0.62</sub>	2.18 <sub>+0.96</sub>	8.73 <sub>-2.33</sub>	10.15 <sub>-1.85</sub>	7.08 <sub>-1.41</sub>	9.91 <sub>-1.69</sub>	9.03 <sub>-1.27</sub>	-1.89 <sub>+0.15</sub>
DS	4/32	3.41 <sub>-0.79</sub>	7.40 <sub>-0.26</sub>	9.01 <sub>+3.90</sub>	4.03 <sub>-0.52</sub>	10.88 <sub>-1.02</sub>	2.41 <sub>+1.19</sub>	8.72 <sub>-2.34</sub>	10.12 <sub>-1.88</sub>	7.15 <sub>-1.48</sub>	9.76 <sub>-1.84</sub>	8.86 <sub>-1.44</sub>	-1.87 <sub>+0.17</sub>
PTQ4DM* [72]	8/8	4.75	9.59	5.16	4.80	13.48	1.20	14.42	15.06	5.31	10.73	11.65	-1.80
Q-Diffusion† [42]	8/8	4.51	8.17	5.21	4.41	12.23	1.62	12.85	14.16	6.01	10.87	10.01	-1.72
PTQD [18]	8/8	3.75	9.89	6.60*	4.89*	14.89*	1.51*	12.76*	13.54*	5.87*	10.69*	10.97*	-1.75*
TM	8/8	3.14 <sub>-0.61</sub>	7.26 <sub>-0.91</sub>	9.12 <sub>+2.52</sub>	4.01 <sub>-0.40</sub>	10.98 <sub>-1.25</sub>	2.53 <sub>+0.91</sub>	8.71 <sub>-4.05</sub>	10.20 <sub>-3.34</sub>	7.21 <sub>+1.20</sub>	9.46 <sub>-1.23</sub>	8.73 <sub>-1.28</sub>	-1.68 <sub>+0.04</sub>
CM	8/8	3.11 <sub>-0.64</sub>	7.12 <sub>-1.05</sub>	9.43 <sub>+2.83</sub>	4.11 <sub>-0.30</sub>	10.82 <sub>-1.41</sub>	2.47 <sub>+0.85</sub>	8.71 <sub>-4.05</sub>	10.18 <sub>-3.36</sub>	7.23 <sub>-1.22</sub>	9.41 <sub>-1.28</sub>	8.69 <sub>-1.32</sub>	-1.66 <sub>+0.06</sub>
DS	8/8	3.08 <sub>-0.67</sub>	7.10 <sub>-1.07</sub>	9.70 <sub>+3.10</sub>	3.97 <sub>-0.44</sub>	10.78 <sub>-1.45</sub>	2.60 <sub>+0.98</sub>	8.71 <sub>-4.05</sub>	10.16 <sub>-3.38</sub>	7.34 <sub>+1.33</sub>	9.35 <sub>-1.34</sub>	8.63 <sub>-1.38</sub>	-1.63 <sub>+0.09</sub>
PTQ4DM [72]	4/8	20.72	54.30	1.42*	4.97*	14.87*	-0.34*	17.08*	17.48*	1.02*	11.83*	12.91*	-3.44*
Q-Diffusion† [42]	4/8	6.40	17.93	3.89	4.66	13.94	0.46	15.55	16.86	2.12	11.45	11.15	-2.94
PTQD [18]	4/8	5.94	15.16	4.42*	5.10*	13.23*	-0.25*	15.47*	17.38*	3.31*	11.42*	11.43*	-3.18*
TM	4/8	3.68 <sub>-2.26</sub>	7.65 <sub>-7.51</sub>	8.02 <sub>+3.60</sub>	4.14 <sub>-0.52</sub>	11.46 <sub>-1.77</sub>	1.97 <sub>+1.51</sub>	8.76 <sub>-6.71</sub>	10.26 <sub>-6.60</sub>	6.78 <sub>-3.47</sub>	9.97 <sub>-1.45</sub>	9.14 <sub>-2.01</sub>	-2.70 <sub>+0.24</sub>
CM	4/8	3.91 <sub>-2.03</sub>	8.61 <sub>-6.55</sub>	7.30 <sub>+2.88</sub>	4.46 <sub>-0.20</sub>	11.39 <sub>-1.84</sub>	1.88 <sub>+1.42</sub>	8.76 <sub>-6.71</sub>	10.18 <sub>-6.68</sub>	6.71 <sub>+3.40</sub>	10.03 <sub>-1.39</sub>	9.11 <sub>-2.04</sub>	-2.71 <sub>+0.23</sub>
DS	4/8	3.61 <sub>-2.33</sub>	7.49 <sub>-7.67</sub>	8.51 <sub>+4.09</sub>	4.13 <sub>-0.53</sub>	10.95 <sub>-2.28</sub>	2.13 <sub>+1.67</sub>	8.73 <sub>-6.74</sub>	10.07 <sub>-6.79</sub>	6.80 <sub>-3.49</sub>	9.81 <sub>-1.61</sub>	9.10 <sub>-2.05</sub>	-2.68 <sub>+0.26</sub>

specifically, in the evaluation process of each experiment, we sample 50k images from DDPM or LDM, 30k images from Stable Diffusion or SD-XL-turbo, and 10K images from SD-XL. All experiments are conducted utilizing one H800 GPU and implemented with the PyTorch framework [62] without special claims.

## 5.2 Performance Comparison

In the experiments conducted on the LDM with DDIM sampler [75], we maintain the same experimental settings as presented in [67], including the number of steps, variance schedule, and classifier-free guidance scale (denoted by eta and cfg in the following, respectively). As shown in Tab. 2, the FID performance differences relative to the full precision (FP) model are all within 0.7 for all settings employing DS. Specifically, on the CelebA-HQ  $256 \times 256$  dataset, DS exhibits an FID reduction of 6.74, an sFID reduction of 6.79, and an SQNR increasing of 4.09 in the w4a8 setting compared to the current algorithms. It is noticeable that existing methods, whether in 4-bit or 8-bit, show significant performance degradation when compared to the FP model on face datasets like CelebA-HQ  $256 \times 256$  and FFHQ  $256 \times 256$ , whereas our TM/CM/DS shows almost no performance degradation. Importantly, DS also achieves significant performance improvement on the LSUN-Bedrooms  $256 \times 256$  in the w4a8 setting, with FID and sFID reductions of 2.33 and 7.67 compared to PTQD [18], respectively. Regarding LDM-8 on LSUN-Churches  $256 \times 256$ , we attribute the moderate improvement, compared to other datasets. We believe that the use of the LDM-8 model with a downsampling factor of 8 may be more quantization-friendly. Existing methods have already achieved satisfactory results on this dataset. Nonetheless, our method still approaches the performance of the FP model more closely than existing methods.

**Unconditional generation.** Besides the experiments on LDM, We have also conducted experiments with DDPM

TABLE 3: Quantization results for unconditional image generation with DDIM on CIFAR-10  $32 \times 32$ .

Methods	#Bits (W/A)	CIFAR-10 $32 \times 32$		
		IS↑	FID↓	SQNR↑
Full Prec.	32/32	9.04	4.23	-
PTQ4DM* [72]	4/32	9.02	5.65	3.68
Q-Diffusion† [42]	4/32	8.78	5.08	4.12
TDQ [74]	4/32	-	-	-
TM	4/32	9.14 <sub>+0.12</sub>	4.73 <sub>-0.35</sub>	5.03 <sub>+0.91</sub>
CM	4/32	9.16 <sub>+0.14</sub>	4.68 <sub>-0.40</sub>	5.21 <sub>+1.09</sub>
DS	4/32	9.21 <sub>+0.19</sub>	4.49 <sub>-0.59</sub>	5.29 <sub>+1.17</sub>
PTQ4DM [72]	8/8	9.02	19.59	4.12*
Q-Diffusion† [42]	8/8	8.89	4.78	4.78
TDQ [74]	8/8	8.85	5.99	-
TM	8/8	9.07 <sub>+0.05</sub>	4.24 <sub>-0.54</sub>	5.67 <sub>+0.89</sub>
CM	8/8	9.05 <sub>+0.03</sub>	4.25 <sub>-0.53</sub>	5.95 <sub>+1.17</sub>
DS	8/8	9.08 <sub>+0.06</sub>	4.18 <sub>-0.61</sub>	5.98 <sub>+1.20</sub>
PTQ4DM* [72]	4/8	8.93	5.14	1.96
Q-Diffusion† [42]	4/8	9.12	4.98	2.07
TDQ [74]	4/8	-	-	-
TM	4/8	9.13 <sub>+0.01</sub>	4.78 <sub>-0.20</sub>	3.43 <sub>+1.36</sub>
CM	4/8	9.13 <sub>+0.01</sub>	4.59 <sub>-0.39</sub>	3.22 <sub>+1.15</sub>
DS	4/8	9.15 <sub>+0.03</sub>	4.46 <sub>-0.52</sub>	3.51 <sub>+1.44</sub>

on CIFAR-10  $32 \times 32$ . As shown in Tab. 3, our methods still achieve comprehensive improvements in terms of IS, FID, and SQNR compared to the existing advanced methods. However, due to the lower resolution and simplicity of the images in this dataset, existing methods show minimal performance degradation, so the results we obtain may not be as pronounced.

**Class-conditional generation.** On the ImageNet  $256 \times 256$  dataset, we employed a denoising process with 20 steps DDIM sampler [75], setting eta and cfg to 0.0 and 3.0, respectively. In Tab. 5, compared to PTQD, our method achieves a FID reduction of 2.09 on w8a8, and a 5.35 sFID decrease on w4a8. Under all the conditions with DS, we observe an improvement of over 9 in IS. Particularly

TABLE 4: Quantization results for text-guided image generation with Stable Diffusion-v1-4, SD-XL-base-1.0, and SD-XL-turbo on MS-COCO captions.

Methods	#Bits (W/A)	Stable Diffusion-v1-4				SD-XL-base-1.0				SD-XL-turbo			
		FID↓	sFID↓	CLIP↑	SQNR↑	FID↓	sFID↓	CLIP↑	SQNR↑	FID↓	sFID↓	CLIP↑	SQNR↑
Full Prec.	32/32	13.15	19.31	31.46	-	34.10	57.03	31.33	-	18.21	28.70	31.74	-
Q-Diffusion+ [42]	4/32	13.58	19.50	31.43	-2.62	28.62	60.34	30.88	1.39	21.75	30.64	31.01	0.02
TM	4/32	<b>13.21</b> <sub>-0.37</sub>	<b>19.03</b> <sub>-0.47</sub>	<b>31.44</b> <sub>+0.01</sub>	<b>5.61</b> <sub>+8.23</sub>	<b>25.82</b> <sub>-2.80</sub>	<b>57.21</b> <sub>-3.13</sub>	<b>31.12</b> <sub>+0.24</sub>	<b>3.74</b> <sub>+2.35</sub>	<b>18.25</b> <sub>-3.50</sub>	<b>29.56</b> <sub>-1.08</sub>	<b>31.01</b> <sub>-0.00</sub>	<b>1.87</b> <sub>+1.85</sub>
CM	4/32	13.22 <sub>-0.36</sub>	<b>19.01</b> <sub>-0.49</sub>	<b>31.44</b> <sub>+0.01</sub>	<b>5.60</b> <sub>+8.22</sub>	<b>26.13</b> <sub>-2.49</sub>	<b>56.71</b> <sub>-3.63</sub>	<b>31.11</b> <sub>+0.23</sub>	<b>3.21</b> <sub>+1.82</sub>	<b>18.56</b> <sub>-3.19</sub>	<b>28.82</b> <sub>-1.82</sub>	<b>31.02</b> <sub>-0.01</sub>	<b>1.98</b> <sub>+1.96</sub>
DS	4/32	<b>13.21</b> <sub>-0.37</sub>	<b>19.01</b> <sub>-0.49</sub>	<b>31.41</b> <sub>+0.04</sub>	<b>5.64</b> <sub>+8.26</sub>	<b>25.63</b> <sub>-2.99</sub>	<b>56.14</b> <sub>-4.20</sub>	<b>31.12</b> <sub>+0.24</sub>	<b>3.87</b> <sub>+2.48</sub>	<b>18.22</b> <sub>-3.53</sub>	<b>28.01</b> <sub>-2.63</sub>	<b>31.04</b> <sub>-0.03</sub>	<b>2.37</b> <sub>+2.35</sub>
Q-Diffusion+ [42]	8/8	13.31	20.54	31.34	-2.60	28.21	60.06	31.15	2.89	21.65	30.71	31.07	1.99
TM	8/8	<b>13.09</b> <sub>-0.22</sub>	<b>19.91</b> <sub>-0.63</sub>	<b>31.34</b> <sub>+0.00</sub>	<b>6.69</b> <sub>+9.29</sub>	<b>25.27</b> <sub>-2.94</sub>	<b>56.36</b> <sub>-3.70</sub>	<b>31.20</b> <sub>+0.05</sub>	<b>5.29</b> <sub>-2.40</sub>	<b>18.08</b> <sub>-3.57</sub>	<b>30.00</b> <sub>-0.71</sub>	<b>31.15</b> <sub>-0.08</sub>	<b>3.58</b> <sub>+1.59</sub>
CM	8/8	13.08 <sub>-0.23</sub>	<b>19.93</b> <sub>-0.61</sub>	<b>31.32</b> <sub>+0.02</sub>	<b>6.62</b> <sub>+9.22</sub>	<b>25.12</b> <sub>-3.09</sub>	<b>56.20</b> <sub>-3.86</sub>	<b>31.22</b> <sub>+0.07</sub>	<b>5.76</b> <sub>+2.87</sub>	<b>18.17</b> <sub>-3.66</sub>	<b>29.41</b> <sub>-1.30</sub>	<b>31.16</b> <sub>-0.09</sub>	<b>3.73</b> <sub>+1.74</sub>
DS	8/8	<b>13.06</b> <sub>-0.25</sub>	<b>19.88</b> <sub>-0.68</sub>	<b>31.30</b> <sub>+0.04</sub>	<b>6.70</b> <sub>+9.30</sub>	<b>25.04</b> <sub>-3.17</sub>	<b>56.12</b> <sub>-3.94</sub>	<b>31.24</b> <sub>+0.09</sub>	<b>5.99</b> <sub>+3.10</sub>	<b>18.02</b> <sub>-3.81</sub>	<b>29.38</b> <sub>-1.33</sub>	<b>31.19</b> <sub>-0.12</sub>	<b>3.97</b> <sub>+1.88</sub>
Q-Diffusion+ [42]	4/8	14.49	20.43	31.21	-2.59	31.18	60.22	31.10	0.88	23.71	30.67	30.98	-0.26
TM	4/8	<b>13.36</b> <sub>-1.13</sub>	<b>20.14</b> <sub>-0.29</sub>	<b>31.28</b> <sub>+0.07</sub>	<b>5.59</b> <sub>+8.15</sub>	<b>25.68</b> <sub>-5.50</sub>	<b>56.95</b> <sub>-3.27</sub>	<b>31.15</b> <sub>+0.05</sub>	<b>3.12</b> <sub>-2.24</sub>	<b>18.24</b> <sub>-5.47</sub>	<b>30.38</b> <sub>-0.29</sub>	<b>31.02</b> <sub>-0.04</sub>	<b>1.64</b> <sub>+1.90</sub>
CM	4/8	13.31 <sub>-1.18</sub>	<b>20.13</b> <sub>-0.31</sub>	<b>31.28</b> <sub>+0.07</sub>	<b>5.56</b> <sub>+8.12</sub>	<b>25.89</b> <sub>-5.29</sub>	<b>56.54</b> <sub>-3.68</sub>	<b>31.13</b> <sub>+0.03</sub>	<b>3.28</b> <sub>-2.40</sub>	<b>18.39</b> <sub>-5.32</sub>	<b>29.48</b> <sub>-1.19</sub>	<b>31.05</b> <sub>-0.07</sub>	<b>1.78</b> <sub>+2.04</sub>
DS	4/8	<b>13.29</b> <sub>-1.20</sub>	<b>20.09</b> <sub>-0.35</sub>	<b>31.30</b> <sub>+0.09</sub>	<b>5.60</b> <sub>+8.16</sub>	<b>25.57</b> <sub>-5.61</sub>	<b>56.42</b> <sub>-3.80</sub>	<b>31.15</b> <sub>+0.05</sub>	<b>3.49</b> <sub>+2.61</sub>	<b>18.21</b> <sub>-5.50</sub>	<b>29.11</b> <sub>-1.56</sub>	<b>31.06</b> <sub>-0.08</sub>	<b>1.82</b> <sub>+2.08</sub>

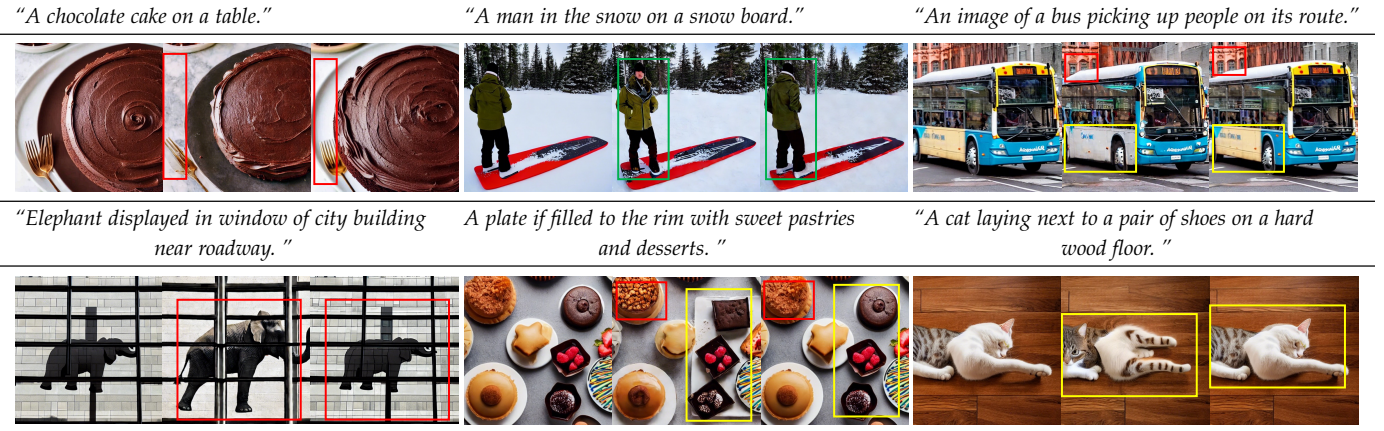


Fig. 8: The images below the corresponding MS-COCO captions are generated from FP (Left), Q-Diffusion (Middle), and our framework (Right) under w4a8 with Stable-Diffusion-v1-4. Different key details are highlighted using rectangles.

TABLE 5: Quantization results for unconditional image generation with class-conditional image generation with LDM-4 on ImageNet 256 × 256.

Methods	#Bits (W/A)	ImageNet 256 × 256			
		IS↑	FID↓	sFID↓	SQNR↑
Full Prec.	32/32	235.64	10.91	7.67	-
PTQ4DM [72]	4/32	-	-	-	-
Q-Diffusion* [42]	4/32	213.56	11.87	8.76	6.16
PTQD+ [18]	4/32	201.78	11.65	9.06	5.97
TM	4/32	223.81 <sub>+10.25</sub>	10.50 <sub>-1.15</sub>	7.98 <sub>-0.78</sub>	<b>8.64</b> <sub>+2.48</sub>
CM	4/32	228.46 <sub>+13.90</sub>	10.42 <sub>-1.23</sub>	8.01 <sub>-0.75</sub>	8.21 <sub>+2.05</sub>
DS	4/32	<b>234.72</b> <sub>+20.16</sub>	<b>10.38</b> <sub>-1.27</sub>	<b>7.81</b> <sub>-0.95</sub>	<b>8.58</b> <sub>+2.42</sub>
PTQ4DM [72]	8/8	161.75	12.59	-	-
Q-Diffusion* [42]	8/8	187.65	12.80	9.87	4.89
PTQD [18]	8/8	153.92	11.94	8.03	5.41
TM	8/8	198.86 <sub>+11.21</sub>	10.79 <sub>-1.15</sub>	7.65 <sub>-0.38</sub>	8.90 <sub>+4.49</sub>
CM	8/8	204.41 <sub>+16.76</sub>	9.99 <sub>-1.95</sub>	7.54 <sub>-0.49</sub>	9.03 <sub>+0.13</sub>
DS	8/8	<b>206.12</b> <sub>+18.47</sub>	<b>9.85</b> <sub>-2.09</sub>	<b>7.52</b> <sub>-0.51</sub>	<b>9.12</b> <sub>+0.22</sub>
PTQ4DM [72]	4/8	-	-	-	-
Q-Diffusion* [42]	4/8	212.51	10.68	14.85	4.02
PTQD [18]	4/8	214.73	10.40	12.63	3.89
TM	4/8	221.82 <sub>+7.09</sub>	10.29 <sub>-0.11</sub>	7.35 <sub>-5.28</sub>	6.78 <sub>+2.76</sub>
CM	4/8	220.01 <sub>+5.28</sub>	9.73 <sub>-0.67</sub>	7.32 <sub>-5.31</sub>	7.01 <sub>+2.99</sub>
DS	4/8	<b>223.97</b> <sub>+9.24</sub>	<b>9.46</b> <sub>-0.94</sub>	<b>7.28</b> <sub>-5.35</sub>	<b>7.03</b> <sub>+3.01</sub>

noteworthy is that, across various quantization settings, our method consistently achieved lower FID and higher SQNR compared to the FP model.

**Text-guided generation.** In this experiment, we generate

high-resolution images of  $512 \times 512$  pixels using Stable Diffusion-v1-4 with 50 steps PLMS sampler [48], and SD-XL-turbo with only a single step Euler sampler [30]. Moreover, higher resolution images of  $1024 \times 1024$  are also generated from SD-XL-base-1.0 with 50 steps Euler sampler. cfg is fixed to the default 7.5 for Stable Diffusion and SD-XL as the trade-off between generation quality and diversity. However, we do not use classifier-free guidance [22] to save memory, the same as the original paper [71]. In Tab. 4, compared to Q-Diffusion, our approach achieves an FID reduction of 1.20, 5.61, and 5.50 under the w4a8 configuration for Stable Diffusion, SD-XL, and SD-XL-turbo, respectively. Notably, our FID on w8a8 and sFID on w4a32 are even lower than those of the full precision model. The table also shows our significantly lower quantization error than Q-Diffusion. For example, DS obtains an 8.16 SQNR upswing for w4a8 Stable Diffusion. Benefiting from this, the visual effect of our generated images<sup>8</sup> is closer to the FP model with better quality than Q-Diffusion (examples in Fig. 8). All of these clues strongly reveal the value of maintaining temporal features.

<sup>8</sup> More qualitative comparisons can be found in the supplementary materials.

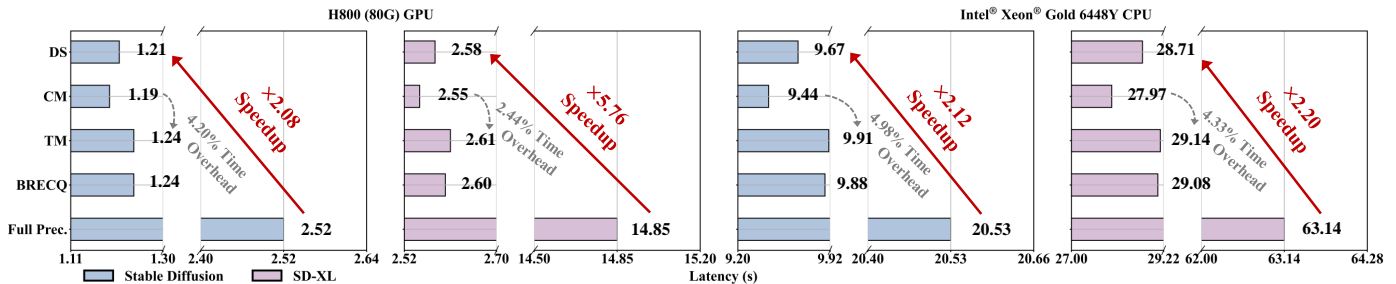


Fig. 9: Latency ablation for Stable Diffusion and SD-XL. BRECCQ [43] is selected as our baseline. We set the batch size to 1 here. Full Prec. is implemented in w32a32 OpenVino and Pytorch.

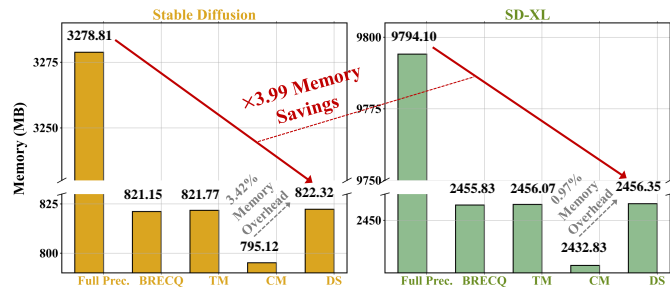


Fig. 10: Memory cost ablation for the UNet in Stable Diffusion and SD-XL.

### 5.3 Efficiency Discussion

In this section, we study the inference efficiency of our quantized diffusion models. In the following, we discuss all components in our quantization framework in the same order as Sec. 4.4.

Specifically, we focus on popular T2I models, *e.g.*, Stable Diffusion-v1-4 [67], SD-XL-base-1.0 [64] with w8a8 quantization and deploy their quantized counterparts on Intel® Xeon® Gold 6448Y Processor with the OpenVino [25] framework. To demonstrate the acceleration on GPU, we also evaluate the latency on Nvidia H800 GPU with quantized convolutions and multiplications harnessing CUTLASS [32] with our customized kernels. An overview can be seen from Fig. 9 and Fig. 10.

#### 5.3.1 Efficiency of TM

First, compared with BRECCQ, our TIB-based Maintenance brings less than 0.08% extra memory consumption, since we employ per-tensor quantization with our FSC for activations. Besides, our strategy only induces an approximated 0.3% speed overhead for Stable Diffusion and SD-XL on CPUs, and the latency comparison results on the GPU also show nearly no difference.

#### 5.3.2 Efficiency of CM

Second, our Cache-based Maintenance removes the necessity to compute temporal features online, which slightly accelerates inference. Specifically, 4.33% speed enhancement for SD-XL on CPU is obtained compared with TM. Note that, CM also requires less storage here, *e.g.*, 26.65MB memory reduction for Stable Diffusion than TM. Even for some models with a large time-steps count like 500 steps LDM on LSUN-Bedroom  $256 \times 256$ , an additional 10.4MB memory

requirement without the TIB brings an extra cost amounting to roughly 3.69% of the quantized UNet size (281.8MB). Moreover, our highly compatible framework can seamlessly integrate step-reduction techniques like advanced sampler or step distillation to further speed up and reduce memory consumption. We leave this for our future study.

#### 5.3.3 Efficiency of DS

Last, equipping with the Disturbance-aware Selection, our complete framework achieves a pronounced efficient inference with significantly lower memory consumption compared with FP. For example, the quantized SD-XL is 5.76 $\times$  faster than the full precision with 3.99 $\times$  memory savings. It is obvious that the time consumption of all different selection results is between TM and CM, so less than a 5% gap between these results is achieved as shown in Fig. 9. Besides, compared to TM in Fig. 10, DS has almost no additional overhead. Based on these analyses, we verify the high efficiency of our framework for inference and deployment.

### 5.4 Ablation Studies

To evaluate the effectiveness of different modules in our proposed method, we perform a thorough ablation study on the LSUN-Bedrooms  $256 \times 256$  dataset with w4a8 quantization, utilizing the LDM-4 model with a DDIM sampler, unless otherwise stated. The basic ablation is shown in Tab. 6.

TABLE 6: The effect of different modules proposed in the paper on LSUN-Bedrooms  $256 \times 256$ . The subscript numbers represent the improvements compared with our baseline. The last 3 rows denote TM, CM, and DS from upper to lower, respectively.

TIB-based Maintenance	Cache-based Maintenance	Disturbance-aware Selection	LSUN-Bedrooms $256 \times 256$		
			FID↓	sFID↓	SQNR↑
Full Prec.			2.98	7.09	-
BRECCQ [43] (Baseline)			9.36	22.73	-1.61
✓			4.84 <sub>-4.52</sub>	9.29 <sub>-13.44</sub>	6.13 <sub>-7.74</sub>
✓	✓		6.07 <sub>-3.29</sub>	11.31 <sub>-11.42</sub>	5.21 <sub>-6.82</sub>
✓	✓	✓	3.68 <sub>-5.68</sub>	7.65 <sub>-15.08</sub>	8.02 <sub>-9.63</sub>
✓	✓	✓	3.91 <sub>-5.45</sub>	8.61 <sub>-14.12</sub>	7.30 <sub>-8.91</sub>
✓	✓	✓	3.61 <sub>-5.75</sub>	7.49 <sub>-15.24</sub>	8.51 <sub>-10.12</sub>

The content is organized as follows. We first explore the effect of TIB-based Maintenance in Sec. 5.4.1. Then, we present detailed calibration ablation for TIB-based Maintenance and Cache-based Maintenance in Sec. 5.4.2 and



Sec. 5.4.3, respectively. Moreover, we evaluate the loss function of Disturbance-aware Selection and detailed analyses of its selection proportion in Sec. 5.4.4 and Sec. 5.4.5. Finally, the performance with advanced samplers is exhibited to further showcase our universality in Sec. 5.4.6.

#### 5.4.1 Effect of TM

As shown in Tab. 6, compared to the baseline method, our TIAR reduces FID and sFID by 4.52 and 13.44, respectively. Additionally, our FSC also achieves promising results. Equipping both approaches can further mitigate performance degradation.

For a more detailed analysis, Fig. 11 (Left) reveals that our methods induce significantly less temporal feature disturbance compared to PTQD. This underscores the efficacy of our motivation and contribution to maintaining temporal features. Further insights are gained by examining the cosine similarity between outputs from the  $i^{\text{th}}$  Residual Bottleneck Blocks pre- and post-quantization. Comparing our methods with PTQD, Fig. 11 (Right) illustrates that our approaches result in significantly lower output errors in the Residual Bottleneck Block. It is also essential to note that these points involve the accumulated errors from multiple denoising iterations in diffusion models. Therefore, Our methods are able to significantly eliminate the accumulative error and quantization error by mitigating temporal feature disturbance within the corresponding block for performance enhancements.

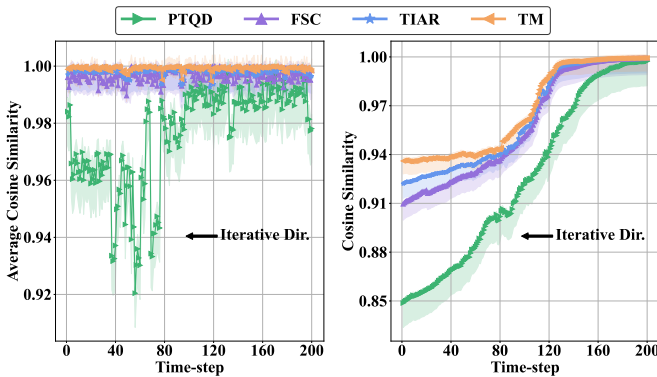


Fig. 11: (Left) Temporal feature errors employing Eq. (8) across different methods. (Right) Cosine similarity of the Residual Bottleneck’s outputs across different PTQ Methods ( $i = 8$ ).

#### 5.4.2 Effect of Calibration Methods for TM

Given the variety of available methods to determine the optimal step size for activations during calibration, we explore several approaches and evaluate both their performance and the GPU time consumed. As detailed in Tab. 7, the performance differences between Min-max and the best-performing ones are minimal, *e.g.*, a mere 0.06 FID gap under w4a8. Therefore, we opt for the simplest and most efficient Min-max [58] as our specific calibration strategy, striking a balance between calibration time and effectiveness. Notably, we have found that PTQD and Q-Diffusion cost 4.68 and 5.29 GPU hours in their PTQ methods under w4a8 quantization, respectively. However, our TIB-based

maintenance only spends 2.32 GPU hours ( $2\times$  speedup) due to our efficient calibration and reconstruction without extra time-consuming compared with previous block/layer-wise reconstruction.

TABLE 7: Different range estimation methods for calibration of TIB-based Maintenance. We report the GPU hours consumed during calibration in the table. Weight reconstruction combined with our TIAR (2.20 GPU hours) is employed before calibration combined with FSC. The subscript numbers represent the improvements between the best-performing methods and Min-max [58].

Methods	#Bits (W/A)	FID↓	sFID↓	SQNR↑	Time
LSQ [11]	8/8	3.17	7.18	<b>9.23</b> <sub>+0.11</sub>	2.48
KL-divergence [56]	8/8	3.27	7.32	9.04	19.67
Percentile [83]	8/8	3.34	7.41	9.09	12.00
MSE [7]	8/8	<b>3.12</b> <sub>-0.02</sub>	<b>7.12</b> <sub>-0.14</sub>	9.09	8.89
Min-max [58]	8/8	3.14	7.26	9.12	<b>0.12</b> <sub>-2.36</sub>
LSQ [11]	4/8	3.69	7.48	<b>8.15</b> <sub>+0.13</sub>	2.57
KL-divergence [56]	4/8	3.94	<b>7.42</b> <sub>-0.23</sub>	8.01	19.65
Percentile [83]	4/8	3.74	8.02	7.98	12.04
MSE [7]	4/8	<b>3.62</b> <sub>-0.06</sub>	7.48	7.99	8.89
Min-max [58]	4/8	3.68	7.65	8.02	<b>0.12</b> <sub>-2.45</sub>

#### 5.4.3 Effect of Calibration Methods for CM

TABLE 8: Different range estimation methods for calibration of Cache-based Maintenance. The subscript numbers represent the improvements between the first and second.

Methods	#Bits (W/A)	FID↓	sFID↓	SQNR↑
LSQ [11]	8/8	<b>3.11</b> <sub>-0.57</sub>	<b>7.12</b> <sub>-0.26</sub>	<b>9.43</b> <sub>+1.11</sub>
KL-divergence [56]	8/8	3.76	7.61	7.58
Percentile [83]	8/8	3.68	7.63	7.89
MSE [7]	8/8	3.62	7.54	8.32
Min-max [58]	8/8	4.41	7.38	6.91
LSQ [11]	4/8	<b>3.91</b> <sub>-0.35</sub>	<b>8.61</b> <sub>-0.41</sub>	<b>7.30</b> <sub>+0.18</sub>
KL-divergence [56]	4/8	4.35	9.02	6.89
Percentile [83]	4/8	4.68	9.42	7.01
MSE [7]	4/8	4.26	9.08	7.12
Min-max [58]	4/8	5.41	10.38	5.02

We also investigate different calibration methods for our Cache-based Maintenance. From Tab. 8, we observe that LSQ outperforms the others, achieving a 13.3% increase in SQNR compared to MSE under w8a8 settings. Hence we choose LSQ as our calibration method. Note that each pre-computed temporal feature can be processed in parallel, enabling the algorithm to achieve rapid runtimes of less than 0.3 hours on a single H800 80G GPU.

#### 5.4.4 Effect of Loss Functions for DS

Since the loss function  $\mathcal{L}_{t,i}^{\text{temporal}}$  in Eq. (14) measures the error of the temporal feature, we assess various loss functions to enhance performance. As shown in Tab. 9, different loss functions produce comparable results, with less than 1% FID and sFID discrepancies among them. Moreover, all results in the table outperform either TIB-based or Cache-based Maintenance in Tab. 2, demonstrating the robustness and effectiveness of the selection strategy.

#### 5.4.5 Effect of Selection Proportion

Beginning with Cache-based Maintenance, we select a proportion of the temporal feature with the lowest  $\tau_{t,i}$  for

TABLE 9: Effect of different loss functions in Eq. (14). We employ MSE [92] align with Eq. (13) in our framework.

Loss Func.	#Bits (W/A)	FID↓	sFID↓	SQNR↑
MSE [92]	8/8	<b>3.08</b> <sub>-0.01</sub>	7.10	9.70
KL [36]	8/8	3.09	7.11	<b>9.85</b> <sub>+0.15</sub>
CE [55]	8/8	3.09	<b>7.07</b> <sub>-0.03</sub>	9.59
MSE [92]	4/8	<b>3.61</b> <sub>-0.02</sub>	<b>7.49</b> <sub>-0.01</sub>	8.51
KL [36]	4/8	3.63	7.56	8.49
CE [55]	4/8	3.64	7.50	<b>8.90</b> <sub>+0.39</sub>

TIB-based Maintenance. Then we increase the proportion progressively until the selection pattern is equivalent to TIB-based Maintenance. As shown in Fig. 12, the lowest FID and highest SQNR achieved by DS compared with other points. Furthermore, selecting maintenance strategies that minimize temporal feature errors can help enhance performance. This investigation also validates our fundamental perspective that temporal feature maintenance is crucial.

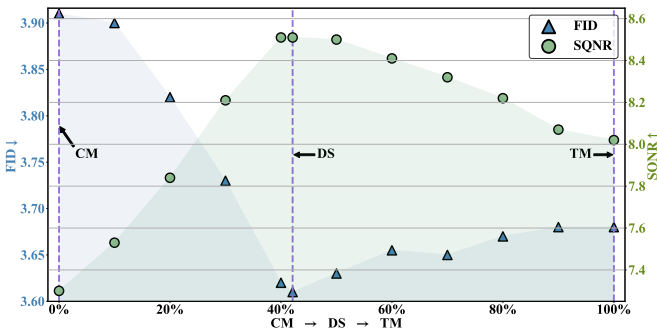


Fig. 12: Performance from Cache-based Maintenance → Disturbance-aware Selection → TIB-based Maintenance. The x-axis represents the proportion of temporal features applied using TIB-based Maintenance.

#### 5.4.6 Generation with Advanced Samplers

Apart from using the DDIM sampler [75], we also utilize a variant of DDPM [21] called PLMS [48] on the CelebA-HQ  $256 \times 256$  dataset [29]. This better demonstrates the superiority of our framework compared to previous works. From Tab. 10, the introduced DS substantially reduces FID and sFID, surpassing PTQD by margins of 12.61 and 7.08, respectively.

TABLE 10: Quantization results for unconditional image generation with PLMS on CelebA-HQ  $256 \times 256$ .

Methods	#Bits (W/A)	CelebA-HQ $256 \times 256$	
		FID↓	sFID↓
Full Prec.	32/32	8.92	10.42
Q-Diffusion [42]	4/8	24.31	22.11
PTQD [18]	4/8	21.08	17.38
DS	4/8	<b>8.47</b> <sub>-12.61</sub>	<b>10.30</b> <sub>-7.08</sub>

Furthermore, we present experiments performed using the DPM++ solver [51] on LSUN-Churches  $256 \times 256$  [85]. As shown in Tab. 11, our framework consistently outperforms existing methods.

TABLE 11: Quantization results for unconditional image generation with DPM++ on LSUN-Churches  $256 \times 256$ .

Methods	#Bits (W/A)	LSUN-Churches $256 \times 256$	
		FID↓	sFID↓
Full Prec.	32/32	4.12	10.55
Q-Diffusion [42]	4/8	7.80	23.24
PTQD [18]	4/8	7.45	22.74
DS	4/8	<b>4.78</b> <sub>-2.67</sub>	<b>11.97</b> <sub>-10.77</sub>

## 6 CONCLUSION & DISCUSSIONS OF LIMITATIONS

In this paper, we have explored the application of quantization to accelerate diffusion models. We have identified a significant and previously unrecognized issue—temporal feature disturbance—in the quantization of diffusion models. Through a detailed analysis, we have pinpointed the root causes of this disturbance and introduced a novel quantization framework to address them. By integrating two maintenance strategies (*i.e.*, TIB-based and Cache-based Maintenance) with our Disturbance-aware Selection, we are able to significantly reduce temporal feature errors. In 4-bit quantization across various datasets and diffusion models, our framework has exhibited minimal performance degradation compared to full-precision models. Moreover, the enhanced inference speed on both GPU and CPU has validated the considerable hardware efficiency of our quantized diffusion model.

However, beyond temporal features, we have discovered that other semantic features introduced in conditional diffusion models possess physical significance and impact the generation effect. Nevertheless, these features are often overlooked in current methodologies. We plan to address this in future research. Furthermore, while temporal feature maintenance is effective in both PTQ and QAT scenarios, our current study focuses primarily on the PTQ setting. Future efforts will extend to the QAT setting to pursue lower-bit quantization and further performance improvements.

## REFERENCES

- [1] S. Agarwal, S. Mitra, S. Chakraborty, S. Karanam, K. Mukherjee, and S. K. Saini. Approximate caching for efficiently serving Text-to-Image diffusion models. In *NSDI*, pages 1173–1189, Santa Clara, CA, Apr. 2024. USENIX Association. 2
- [2] F. Bao, C. Li, J. Sun, J. Zhu, and B. Zhang. Estimating the optimal covariance with imperfect mean in diffusion probabilistic models. In *ICML*, volume 162, pages 1555–1584, 2022. 2
- [3] F. Bao, C. Li, J. Zhu, and B. Zhang. Analytic-dpm: an analytic estimate of the optimal reverse variance in diffusion probabilistic models. In *ICLR*, 2022. 2
- [4] Y. Bhalgat, J. Lee, M. Nagel, T. Blankevoort, and N. Kwak. Lsq+: Improving low-bit quantization through learnable offsets and better initialization, 2020. 1, 7
- [5] T. B. Brown, B. Mann, N. Ryder, M. Subbiah, J. Kaplan, P. Dhariwal, A. Neelakantan, P. Shyam, G. Sastry, A. Askell, S. Agarwal, A. Herbert-Voss, G. Krueger, T. Henighan, R. Child, A. Ramesh, D. M. Ziegler, J. Wu, C. Winter, C. Hesse, M. Chen, E. Sigler, M. Litwin, S. Gray, B. Chess, J. Clark, C. Berner, S. McCandlish, A. Radford, I. Sutskever, and D. Amodei. Language models are few-shot learners, 2020. 1
- [6] Y.-H. Chen, R. Sarokin, J. Lee, J. Tang, C.-L. Chang, A. Kulik, and M. Grundmann. Speed is all you need: On-device acceleration of large diffusion models via gpu-aware optimizations. In *CVPR*, pages 4651–4655, 2023. 1
- [7] Y. Choukroun, E. Kravchik, F. Yang, and P. Kisilev. Low-bit quantization of neural networks for efficient inference. In *ICCVW*, pages 3009–3018. IEEE, 2019. 11

- [8] H. Chung, B. Sim, and J. C. Ye. Come-closer-diffuse-faster: Accelerating conditional diffusion models for inverse problems through stochastic contraction. In *CVPR*, pages 12413–12422, 2022. **2**
- [9] J. Deng, W. Dong, R. Socher, L.-J. Li, K. Li, and L. Fei-Fei. Imagenet: A large-scale hierarchical image database. In *CVPR*, pages 248–255. Ieee, 2009. **7**
- [10] A. Dosovitskiy, L. Beyer, A. Kolesnikov, D. Weissenborn, X. Zhai, T. Unterthiner, M. Dehghani, M. Minderer, G. Heigold, S. Gelly, et al. An image is worth 16x16 words: Transformers for image recognition at scale. *arXiv preprint arXiv:2010.11929*, 2020. **7**
- [11] S. K. Esser, J. L. McKinstry, D. Bablani, R. Appuswamy, and D. S. Modha. Learned step size quantization. In *ICLR*, 2020. **1, 6, 11**
- [12] E. Frantar and D. Alistarh. Optimal brain compression: A framework for accurate post-training quantization and pruning. *NeurIPS*, 35:4475–4488, 2022. **3**
- [13] G. Franzese, S. Rossi, L. Yang, A. Finamore, D. Rossi, M. Filippone, and P. Michiardi. How much is enough? a study on diffusion times in score-based generative models. *arXiv preprint arXiv:2206.05173*, 2022. **2**
- [14] R. Gong, X. Liu, S. Jiang, T. Li, P. Hu, J. Lin, F. Yu, and J. Yan. Differentiable soft quantization: Bridging full-precision and low-bit neural networks. In *ICCV*, pages 4852–4861, 2019. **1, 2**
- [15] I. Goodfellow, J. Pouget-Abadie, M. Mirza, B. Xu, D. Warde-Farley, S. Ozair, A. Courville, and Y. Bengio. Generative adversarial networks. *Communications of the ACM*, 63(11):139–144, 2020. **1**
- [16] S. Han, J. Pool, J. Tran, and W. Dally. Learning both weights and connections for efficient neural network. In C. Cortes, N. Lawrence, D. Lee, M. Sugiyama, and R. Garnett, editors, *NeurIPS*, volume 28. Curran Associates, Inc., 2015. **7**
- [17] Y. He, J. Liu, W. Wu, H. Zhou, and B. Zhuang. Efficientdm: Efficient quantization-aware fine-tuning of low-bit diffusion models. In *ICLR*, 2024. **7**
- [18] Y. He, L. Liu, J. Liu, W. Wu, H. Zhou, and B. Zhuang. Ptdq: Accurate post-training quantization for diffusion models. In *NeurIPS*, 2023. **2, 3, 5, 7, 8, 9, 12**
- [19] J. Hessel, A. Holtzman, M. Forbes, R. L. Bras, and Y. Choi. Clipsecore: A reference-free evaluation metric for image captioning, 2022. **7**
- [20] M. Heusel, H. Ramsauer, T. Unterthiner, B. Nessler, and S. Hochreiter. Gans trained by a two time-scale update rule converge to a local nash equilibrium, 2018. **1, 4, 7**
- [21] J. Ho, A. Jain, and P. Abbeel. Denoising diffusion probabilistic models. In *NeurIPS*, 2020. **1, 3, 7, 12**
- [22] J. Ho and T. Salimans. Classifier-free diffusion guidance, 2022. **1, 9**
- [23] Y. Huang, R. Gong, J. Liu, T. Chen, and X. Liu. Tfmq-dm: Temporal feature maintenance quantization for diffusion models. In *CVPR*, pages 7362–7371, June 2024. **2, 5**
- [24] I. Hubara, Y. Nahshan, Y. Hanani, R. Banner, and D. Soudry. Improving post training neural quantization: Layer-wise calibration and integer programming. *arXiv preprint arXiv:2006.10518*, 2020. **1, 2, 3**
- [25] Intel. Openvino. <https://github.com/openvinotoolkit/openvino>, 2018. **2, 10**
- [26] B. Jacob, S. Kligys, B. Chen, M. Zhu, M. Tang, A. Howard, H. Adam, and D. Kalenichenko. Quantization and training of neural networks for efficient integer-arithmetic-only inference. In *CVPR*, pages 2704–2713, 2018. **2, 7**
- [27] A. Jolicœur-Martineau, K. Li, R. Piché-Taillefer, T. Kachman, and I. Mitliagkas. Gotta go fast when generating data with score-based models. *arXiv preprint arXiv:2105.14080*, 2021. **2**
- [28] M. Kang, J.-Y. Zhu, R. Zhang, J. Park, E. Shechtman, S. Paris, and T. Park. Scaling up gans for text-to-image synthesis, 2023. **1**
- [29] T. Karras, T. Aila, S. Laine, and J. Lehtinen. Progressive growing of gans for improved quality, stability, and variation, 2018. **7, 12**
- [30] T. Karras, M. Aittala, T. Aila, and S. Laine. Elucidating the design space of diffusion-based generative models, 2022. **9**
- [31] T. Karras, S. Laine, and T. Aila. A style-based generator architecture for generative adversarial networks, 2019. **1, 7**
- [32] A. Kerr, D. Merrill, J. Demouth, and J. Tran. Cutlass: Fast linear algebra in cuda c++. *NVIDIA Developer Blog*, 2017. **2, 10**
- [33] B. Kim and J. C. Ye. Denoising mcmc for accelerating diffusion-based generative models. *arXiv preprint arXiv:2209.14593*, 2022. **2**
- [34] B.-K. Kim, H.-K. Song, T. Castells, and S. Choi. Bk-sdm: A lightweight, fast, and cheap version of stable diffusion. *arXiv e-prints*, pages arXiv–2305, 2023. **2**
- [35] G. Kim, B. Kim, E. Park, and S. Cho. Task-oriented diffusion model compression, 2024. **2**
- [36] T. Kim, J. Oh, N. Kim, S. Cho, and S.-Y. Yun. Comparing kullback-leibler divergence and mean squared error loss in knowledge distillation. *arXiv preprint arXiv:2105.08919*, 2021. **12**
- [37] D. Kingma, T. Salimans, B. Poole, and J. Ho. Variational diffusion models. In *NeurIPS*, pages 21696–21707, 2021. **2**
- [38] D. P. Kingma and M. Welling. Auto-encoding variational bayes, 2022. **1**
- [39] Z. Kong and W. Ping. On fast sampling of diffusion probabilistic models. *arXiv preprint arXiv:2106.00132*, 2021. **1, 2**
- [40] A. Krizhevsky. Learning multiple layers of features from tiny images. *University of Toronto*, 05 2012. **7**
- [41] M. W. Y. Lam, J. Wang, D. Su, and D. Yu. BDDM: bilateral denoising diffusion models for fast and high-quality speech synthesis. In *ICLR*, 2022. **2**
- [42] X. Li, L. Lian, Y. Liu, H. Yang, Z. Dong, D. Kang, S. Zhang, and K. Keutzer. Q-diffusion: Quantizing diffusion models. In *ICCV*, 2023. **1, 2, 3, 5, 7, 8, 9, 12**
- [43] Y. Li, R. Gong, X. Tan, Y. Yang, P. Hu, Q. Zhang, F. Yu, W. Wang, and S. Gu. BRECCO: pushing the limit of post-training quantization by block reconstruction. In *ICLR*, 2021. **1, 2, 3, 5, 7, 10**
- [44] Z. Li, C. Guo, Z. Zhu, Y. Zhou, Y. Qiu, X. Gao, J. Leng, and M. Guo. Efficient adaptive activation rounding for post-training quantization. *arXiv preprint arXiv:2208.11945*, 2022. **3**
- [45] T.-Y. Lin, M. Maire, S. Belongie, L. Bourdev, R. Girshick, J. Hays, P. Perona, D. Ramanan, C. L. Zitnick, and P. Dollár. Microsoft coco: Common objects in context, 2015. **7**
- [46] Y. Lin, T. Zhang, P. Sun, Z. Li, and S. Zhou. Fq-vit: Post-training quantization for fully quantized vision transformer. In *IJCAI*, pages 1173–1179, 2022. **2**
- [47] J. Liu, L. Niu, Z. Yuan, D. Yang, X. Wang, and W. Liu. Pd-quant: Post-training quantization based on prediction difference metric. In *CVPR*, pages 24427–24437, 2023. **3**
- [48] L. Liu, Y. Ren, Z. Lin, and Z. Zhao. Pseudo numerical methods for diffusion models on manifolds. In *ICLR*, 2022. **1, 2, 9, 12**
- [49] C. Louizos, M. Reisser, T. Blankevoort, E. Gavves, and M. Welling. Relaxed quantization for discretized neural networks. In *ICLR*, 2019. **2**
- [50] C. Lu, Y. Zhou, F. Bao, J. Chen, C. Li, and J. Zhu. Dpm-solver: A fast ODE solver for diffusion probabilistic model sampling in around 10 steps. In *NeurIPS*, 2022. **1, 2**
- [51] C. Lu, Y. Zhou, F. Bao, J. Chen, C. Li, and J. Zhu. Dpm-solver++: Fast solver for guided sampling of diffusion probabilistic models, 2023. **12**
- [52] E. Luhman and T. Luhman. Knowledge distillation in iterative generative models for improved sampling speed. *arXiv preprint arXiv:2101.02388*, 2021. **2**
- [53] Z. Lyu, X. Xu, C. Yang, D. Lin, and B. Dai. Accelerating diffusion models via early stop of the diffusion process. *arXiv preprint arXiv:2205.12524*, 2022. **2**
- [54] X. Ma, G. Fang, and X. Wang. Deepcache: Accelerating diffusion models for free. In *CVPR*, pages 15762–15772, 2024. **1**
- [55] A. Mao, M. Mohri, and Y. Zhong. Cross-entropy loss functions: Theoretical analysis and applications. In *ICLR*, pages 23803–23828. PMLR, 2023. **12**
- [56] S. Migacz. Nvidia 8-bit inference with tensorrt. *GPU Technology Conference*, 2017. **11**
- [57] M. Nagel, R. A. Amjad, M. van Baalen, C. Louizos, and T. Blankevoort. Up or down? adaptive rounding for post-training quantization. In *ICML*, volume 119, pages 7197–7206, 2020. **1, 2, 3, 7**
- [58] M. Nagel, M. Fournarakis, R. A. Amjad, Y. Bondarenko, M. van Baalen, and T. Blankevoort. A white paper on neural network quantization, 2021. **1, 5, 6, 11**
- [59] T. H. Nguyen and A. Tran. Swiftbrush: One-step text-to-image diffusion model with variational score distillation. In *CVPR*, pages 7807–7816, 2024. **2**
- [60] A. Q. Nichol and P. Dhariwal. Improved denoising diffusion probabilistic models. In *ICML*, pages 8162–8171, 2021. **2, 3**
- [61] N. P. Pandey, M. Fournarakis, C. Patel, and M. Nagel. Softmax bias correction for quantized generative models, 2023. **7**
- [62] A. Paszke, S. Gross, F. Massa, A. Lerer, J. Bradbury, G. Chanan, T. Killeen, Z. Lin, N. Gimelshein, L. Antiga, et al. Pytorch: An imperative style, high-performance deep learning library. *NeurIPS*, 32, 2019. **8**



- [63] W. Peebles and S. Xie. Scalable diffusion models with transformers. In *ICCV*, pages 4195–4205, 2023. [3](#)
- [64] D. Podell, Z. English, K. Lacey, A. Blattmann, T. Dockhorn, J. Müller, J. Penna, and R. Rombach. Sdxl: Improving latent diffusion models for high-resolution image synthesis, 2023. [1](#), [2](#), [7](#), [10](#)
- [65] M. Rastegari, V. Ordonez, J. Redmon, and A. Farhadi. Xnornet: Imagenet classification using binary convolutional neural networks. In *ECCV*, pages 525–542, 2016. [7](#)
- [66] Y. Ren, C. Hu, X. Tan, T. Qin, S. Zhao, Z. Zhao, and T.-Y. Liu. Fastspeech 2: Fast and high-quality end-to-end text to speech, 2022. [1](#)
- [67] R. Rombach, A. Blattmann, D. Lorenz, P. Esser, and B. Ommer. High-resolution image synthesis with latent diffusion models. In *CVPR*, 2022. [1](#), [7](#), [8](#), [10](#)
- [68] O. Ronneberger, P. Fischer, and T. Brox. U-net: Convolutional networks for biomedical image segmentation, 2015. [3](#)
- [69] T. Salimans, I. Goodfellow, W. Zaremba, V. Cheung, A. Radford, and X. Chen. Improved techniques for training gans, 2016. [7](#)
- [70] T. Salimans and J. Ho. Progressive distillation for fast sampling of diffusion models. In *ICLR*, 2022. [2](#)
- [71] A. Sauer, D. Lorenz, A. Blattmann, and R. Rombach. Adversarial diffusion distillation. *arXiv preprint arXiv:2311.17042*, 2023. [1](#), [2](#), [7](#), [9](#)
- [72] Y. Shang, Z. Yuan, B. Xie, B. Wu, and Y. Yan. Post-training quantization on diffusion models. In *CVPR*, 2023. [2](#), [3](#), [8](#), [9](#)
- [73] J. Shen, R. Pang, R. J. Weiss, M. Schuster, N. Jaitly, Z. Yang, Z. Chen, Y. Zhang, Y. Wang, R. Skerry-Ryan, R. A. Saurous, Y. Agiomyriakakis, and Y. Wu. Natural tts synthesis by conditioning wavenet on mel spectrogram predictions, 2018. [1](#)
- [74] J. So, J. Lee, D. Ahn, H. Kim, and E. Park. Temporal dynamic quantization for diffusion models. In *NeurIPS*, 2023. [2](#), [3](#), [5](#), [7](#), [8](#)
- [75] J. Song, C. Meng, and S. Ermon. Denoising diffusion implicit models. In *ICLR*, 2021. [1](#), [2](#), [3](#), [8](#), [12](#)
- [76] Y. Song, J. Sohl-Dickstein, D. P. Kingma, A. Kumar, S. Ermon, and B. Poole. Score-based generative modeling through stochastic differential equations. In *ICLR*, 2021. [2](#)
- [77] C. Wang, Z. Wang, X. Xu, Y. Tang, J. Zhou, and J. Lu. Towards accurate data-free quantization for diffusion models. *arXiv preprint arXiv:2305.18723*, 2023. [2](#), [3](#), [5](#)
- [78] H. Wang, Y. Shang, Z. Yuan, J. Wu, and Y. Yan. Quest: Low-bit diffusion model quantization via efficient selective finetuning, 2024. [7](#)
- [79] P. Wang, Q. Chen, X. He, and J. Cheng. Towards accurate post-training network quantization via bit-split and stitching. In *ICML*, pages 9847–9856, 2020. [3](#)
- [80] D. Watson, W. Chan, J. Ho, and M. Norouzi. Learning fast samplers for diffusion models by differentiating through sample quality. In *ICLR*, 2022. [2](#)
- [81] X. Wei, R. Gong, Y. Li, X. Liu, and F. Yu. Qdrop: Randomly dropping quantization for extremely low-bit post-training quantization. In *ICLR*, 2022. [1](#), [2](#), [3](#)
- [82] F. Wimbauer, B. Wu, E. Schoenfeld, X. Dai, J. Hou, Z. He, A. Sanakoyeu, P. Zhang, S. Tsai, J. Kohler, et al. Cache me if you can: Accelerating diffusion models through block caching. In *CVPR*, pages 6211–6220, 2024. [2](#)
- [83] H. Wu, P. Judd, X. Zhang, M. Isaev, and P. Micikevicius. Integer quantization for deep learning inference: Principles and empirical evaluation. *arXiv preprint arXiv:2004.09602*, 2020. [11](#)
- [84] X. Yang, D. Zhou, J. Feng, and X. Wang. Diffusion probabilistic model made slim. In *CVPR*, pages 22552–22562, 2023. [1](#)
- [85] F. Yu, A. Seff, Y. Zhang, S. Song, T. Funkhouser, and J. Xiao. Lsun: Construction of a large-scale image dataset using deep learning with humans in the loop, 2016. [4](#), [5](#), [7](#), [12](#)
- [86] L. Zhang, Y. He, Z. Lou, X. Ye, Y. Wang, and H. Zhou. Root quantization: a self-adaptive supplement ste. *Applied Intelligence*, 53(6):6266–6275, 2023. [2](#)
- [87] Q. Zhang and Y. Chen. Fast sampling of diffusion models with exponential integrator. *arXiv preprint arXiv:2204.13902*, 2022. [2](#)
- [88] Q. Zhang, M. Tao, and Y. Chen. gddim: Generalized denoising diffusion implicit models. *arXiv preprint arXiv:2206.05564*, 2022. [2](#)
- [89] S. Zhang, S. Roller, N. Goyal, M. Artetxe, M. Chen, S. Chen, C. Dewan, M. Diab, X. Li, X. V. Lin, T. Mihaylov, M. Ott, S. Shleifer, K. Shuster, D. Simig, P. S. Koura, A. Sridhar, T. Wang, and L. Zettlemoyer. Opt: Open pre-trained transformer language models, 2022. [1](#)
- [90] Y. Zhao, Y. Xu, Z. Xiao, and T. Hou. Mobilediffusion: Subsecond text-to-image generation on mobile devices. *arXiv preprint arXiv:2311.16567*, 2023. [1](#)
- [91] H. Zheng, P. He, W. Chen, and M. Zhou. Truncated diffusion probabilistic models. *stat*, 1050:7, 2022. [2](#)
- [92] J. Zhou, X. Li, T. Ding, C. You, Q. Qu, and Z. Zhu. On the optimization landscape of neural collapse under MSE loss: Global optimality with unconstrained features. In K. Chaudhuri, S. Jegelka, L. Song, C. Szepesvari, G. Niu, and S. Sabato, editors, *ICML*, volume 162 of *Proceedings of Machine Learning Research*, pages 27179–27202. PMLR, 17–23 Jul 2022. [12](#)
- [93] B. Zhuang, C. Shen, M. Tan, L. Liu, and I. Reid. Towards effective low-bitwidth convolutional neural networks. In *CVPR*, pages 7920–7928, 2018. [2](#)

## Supplementary Material for “Temporal Feature Matters: A Framework for Diffusion Model Quantization”

In this supplementary material, we present random samples derived from FP and w4a8 quantized diffusion models with a fixed random seed. These quantized models were created through our complete framework or previous methods. As shown from Fig. I to Fig. IX, our framework yields results that closely resemble those of the FP model, showcasing higher fidelity. Moreover, it excels in finer details, producing superior outcomes in some intricate aspects (zoom in to closely examine the relevant images).



Fig. I: Random samples from w4a8 quantized and FP LDM-4 on CelebA-HQ  $256 \times 256$ . The resolution of each sample is  $256 \times 256$ .

Fig. II: Random samples from w4a8 quantized and FP LDM-4 on FFHQ  $256 \times 256$ . The resolution of each sample is  $256 \times 256$ .

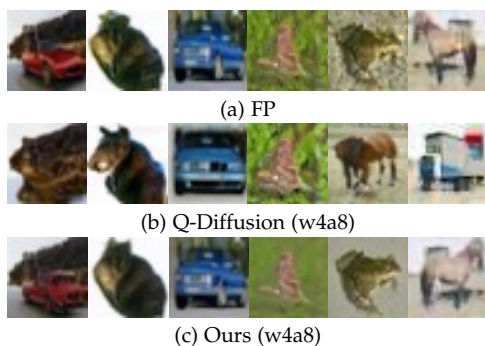


Fig. III: Random samples from w4a8 quantized and FP DDIM on CIFAR-10  $32 \times 32$ . The resolution of each sample is  $32 \times 32$ .



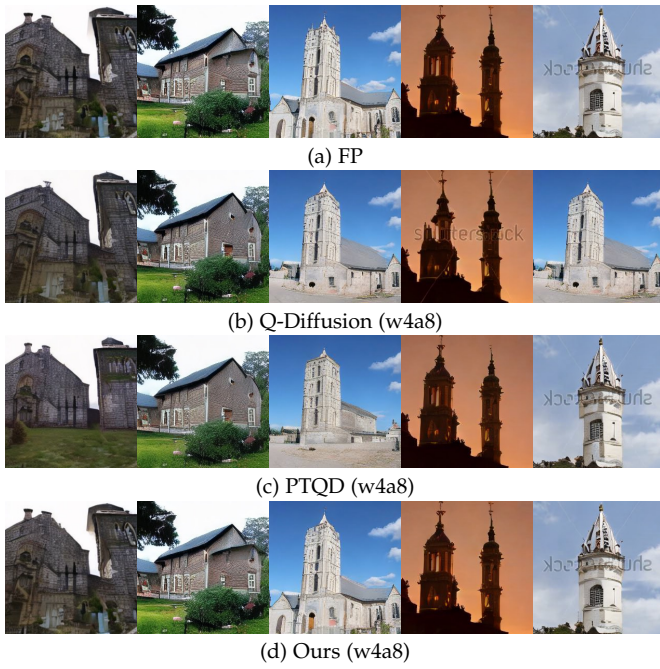


Fig. IV: Random samples from w4a8 quantized and FP LDM-8 on LSUN-Churches  $256 \times 256$ . The resolution of each sample is  $256 \times 256$ .

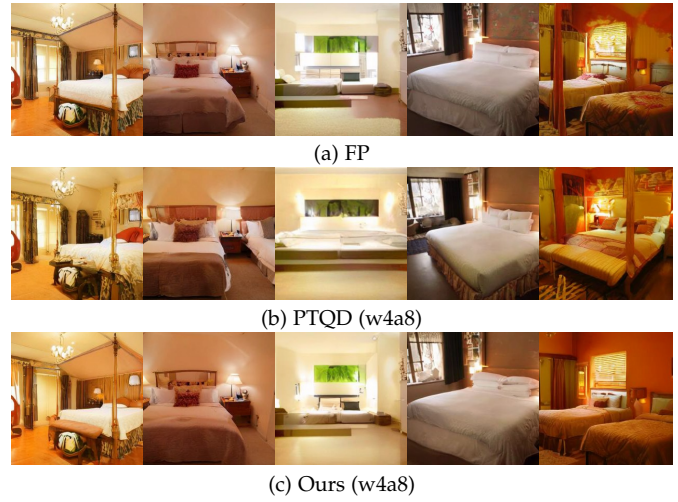


Fig. V: Random samples from w4a8 quantized and FP LDM-4 on LSUN-Bedrooms  $256 \times 256$ . The resolution of each sample is  $256 \times 256$ .

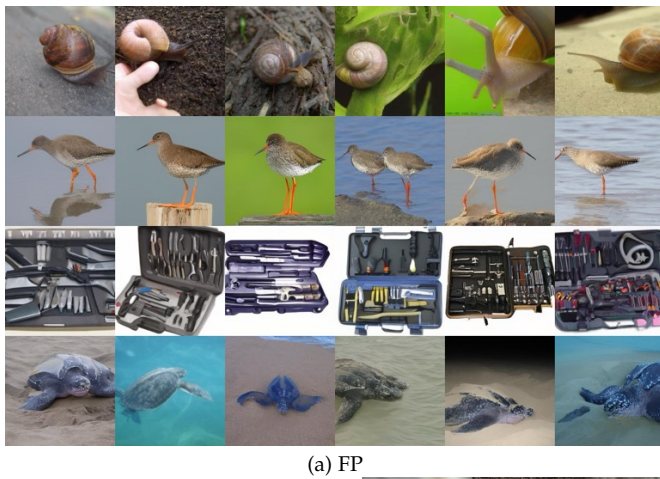


Fig. VI: Random samples from w4a8 quantized and FP LDM-4 on ImageNet  $256 \times 256$ . The resolution of each sample is  $256 \times 256$ .





Fig. VII: Random samples from w4a8 quantized and FP Stable Diffusion-v1-4 on MS-COCO captions. The resolution of each sample is  $512 \times 512$ . The images below the corresponding prompts are generated from FP (Left), Q-Diffusion (Middle), and our framework (Right).

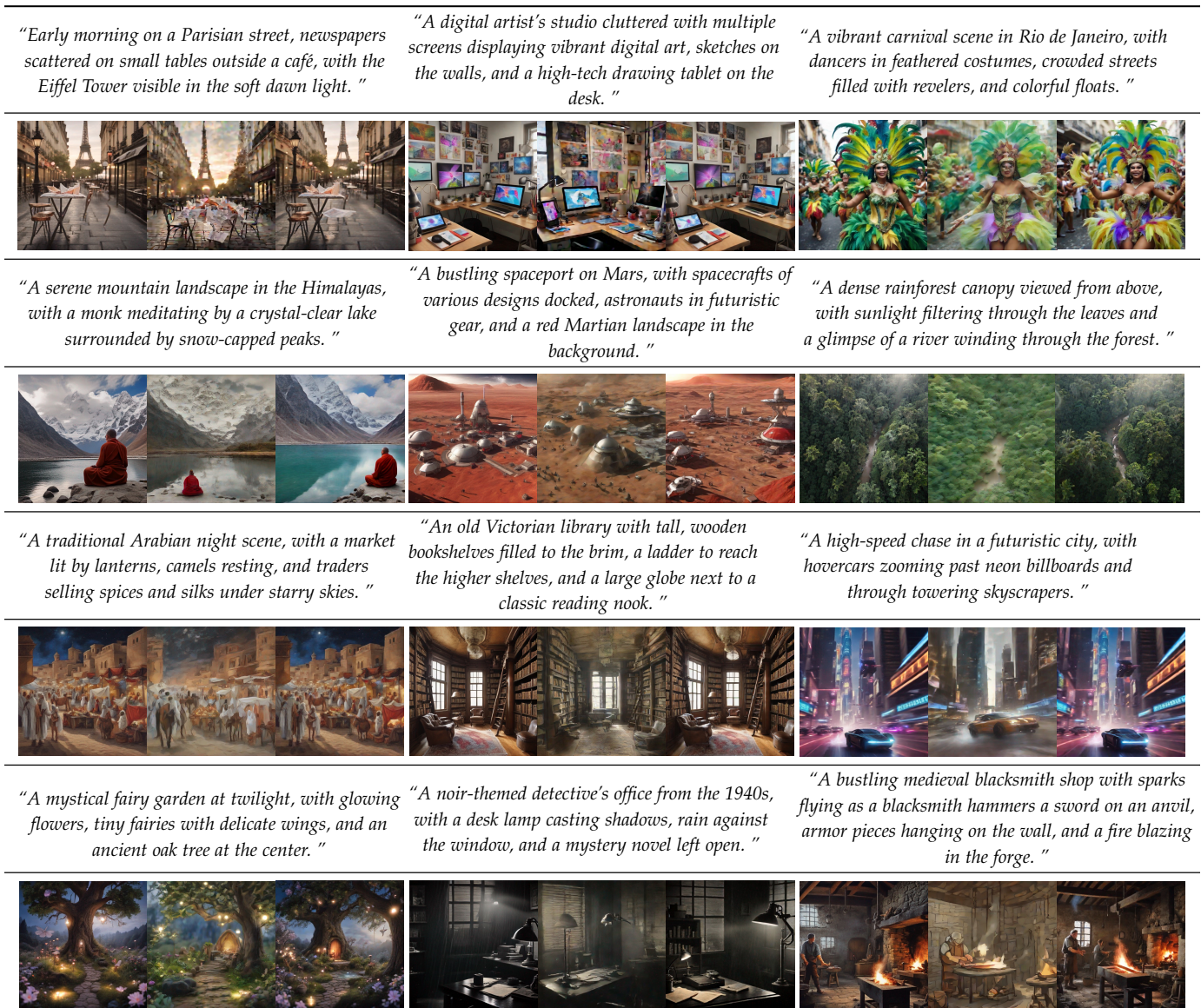


Fig. VIII: Random samples from w4a8 quantized and FP SD-XL-turbo. The resolution of each sample is  $512 \times 512$ . The images below the corresponding prompts are generated from FP (Left), Q-Diffusion (Middle), and our framework (Right).



*"A surreal landscape featuring a giant clock melting over a cliff, under a sky filled with swirling clouds and two suns, reminiscent of Salvador Dali's style."*



*"A bustling medieval market scene with vendors selling colorful spices and textiles, horses and carts in the background, and a castle on a hill in the distance."*



*"A futuristic cityscape at night, illuminated by neon lights, with flying cars zooming between high-rise buildings that have gardens growing on their roofs."*



*"An underwater scene showing a coral reef with a variety of colorful fish, a sunken pirate ship in the background, and light filtering through the water from above."*



*"A scene from a fantasy novel showing a wizard casting a spell in a library full of ancient books, with magical symbols glowing in the air around him."*



*"A serene autumn landscape in a Japanese garden with a red bridge over a pond filled with koi fish, surrounded by maple trees with leaves changing color."*



*"An action-packed scene from a superhero comic book showing a hero in a bright costume flying above a city, chasing a villain who is escaping on a high-tech motorcycle."*



*"A traditional African village at sunset, with round mud huts, people dressed in colorful clothing, and a large baobab tree in the center of the village."*



Fig. IX: Random samples from w4a8 quantized and FP SD-XL. The resolution of each sample is  $1024 \times 1024$ . The images below the corresponding prompts are generated from FP (Left), Q-Diffusion (Middle), and our framework (Right).